Milankovitch Cyclicity and Global Time Constraint of Cretaceous Black Shales and Oceanic Anoxic Event 2 at the Demerara Rise, Western Equatorial Atlantic Ocean

A thesis submitted in partial fulfillment of the requirements for the degree of Master of Science at George Mason University

By

Sean E. Karoly
Bachelor of Science
Radford University, 2015

Director: Linda A. Hinnov, Professor
Department of Atmospheric, Oceanic, and Earth Sciences

Summer Semester 2017
George Mason University
Fairfax, VA

ACKNOWLEDGEMENTS

I first want to thank Drs. Brad Sageman, Mark Leckie, Richard Barclay, and Michael A. Arthur for leading the GSA Field Trip on Cretaceous ocean-climate perturbations revealed in the Cenomanian-Campanian strata of Colorado, and providing a hands-on experience for me to fully appreciate the time period in which my thesis research took place. I would like to thank Dr. Steve Meyers from the University of Wisconsin for his help at the 2016 Isoastro Workshop. I would like to thank Drs. Sean Higgins from the Lamont-Doherty Earth Observatory and Anders Noren from LacCore at the University of Minnesota for taking their time to respond to every question I had about using Correlator. I would like to thank Andy Fraass from the Smithsonian Institution for his input on the microbiological aspects of this thesis. I would also like to extend my appreciation to my lab members and colleagues: Damien Pas, Chao Ma, and M'bark Baddouh, for their advice and assistance as I progressed through my thesis. I would like to thank my parents for providing me support not only during my thesis, but for my entire life. I would last like to acknowledge my advisor, Dr. Linda A. Hinnov, for picking up yet another graduate student in addition to her already busy schedule, and spending countless hours on this project.

TABLE OF CONTENTS

LIST OF TABLES

Page

Table

LIST OF FIGURES

ABSTRACT

MILANKOVITCH CYCLICITY AND GLOBAL TIME CONSTRAINT OF CRETACEOUS BLACK SHALES AND OCEANIC ANOXIC EVENT 2 AT THE DEMERARA RISE, WESTERN EQUATORIAL ATLANTIC OCEAN

Sean E. Karoly, M.S.

George Mason University, 2017

Thesis Director: Dr. Linda A. Hinnov

Testing for Milankovitch cycles in stratigraphy enables observations of astronomical forcing impacts on climate change, sedimentary cyclicity, carbon sequestration, and climatic effects on organisms. Since Milankovitch cycles are global in nature, their recognition in stratigraphy also provides a means for geologic time determination and high-resolution global correlation. Here this testing is applied to the organic black marine shales at the Demerara Rise (western equatorial Atlantic Ocean) deposited during Oceanic Anoxic Event 2 (OAE2) delineating the Cenomanian-Turonian boundary in the early Late Cretaceous period. Stratigraphic correlation of the Demerara Rise to OAE2-age sediment in the Western Interior Seaway and North Atlantic and Tethys oceans relies largely on inconsistent biostratigraphy and chemostratigraphy, in particular a large, positive marine carbon isotope excursion (CIE). High-resolution grayscale data from Ocean Drilling Program Leg 207 drill cores at the Demerara Rise

depict millimeter to meter scale sedimentological variations before, during, and after OAE2 that can be correlated to the CIE. Superimposed meter-scale cyclicity in the grayscale stratigraphic series provides evidence for Milankovitch forcing, and leads to new key refinements in the time-series analysis and global correlation of OAE2.

INTRODUCTION

Oceanic Anoxic Event 2 (OAE2) marks a time interval in the early Late Cretaceous period of significant warming, high sea levels, and an extreme excursion in the global carbon cycle (Schlanger and Jenkyns, 1976; Arthur et al., 1988; Meyers et al., 2012a, among many others). These characteristics can be observed globally, in present-day outcrop sites in Pueblo, Colorado, Eastbourne, southern United Kingdom, and the Tarfaya Basin in southern Morocco (Eldrett et al., 2014; Tsikos et al., 2004; Keller et al., 2008). In Italy, the well-known “Livello Bonarelli” has been biostratigraphically linked to OAE2 (Alvarez and Sannipoli, 2016).

During the OAE2 time interval, which includes the Cenomanian-Turonian (C-T) boundary at 93.9 ± 0.1 Ma (Meyers et al., 2012a), increased accumulation of organic-rich sediments occurred with a distinctly rhythmic behavior. This cyclic deposition is thought to be Milankovitchian (Nederbragt et al., 2007; Meyers et al., 2012b). One importantly situated location where these cycles and associated geochemical variations can be studied is the Demerara Rise in the western equatorial Atlantic Ocean. Exploration at this site began in 2002 by the Ocean Drilling Program (ODP; Erbacher et al., 2004a). The ODP drilled five sites at this location to gain insight on how the opening of the equatorial Atlantic Ocean gateway played a role in the deposition of Cretaceous black shales, and influenced heat transport and circulation (Figure 1; Shipboard Scientific Party, 2004).

A number of sediment proxies have been used to study global climate during OAE2, notably stable carbon isotopes from organic matter ($\delta^{13}C_{org}$) and biostratigraphy of microfossils deposited during times of elevated oceanic anoxia (Erbacher et al., 2005; Eldrett et al., 2014; Hardas and Mutterlose 2006; Friedrich et al., 2006). However, using Milankovitch cycles as a global parameter is not currently well documented for OAE2. Digital grayscale scans of OAE2 sediment core photographs provide an excellent and affordable method to examine the presence of Milankovitch cycles where cyclic changes in climate-forced sediment deposition can often be observed as changes in sediment composition or microfossil deposition, as they impact the color of sediment (Nederbragt et al., 2007). These changes are especially prominent in the organic black shales of the Demerara Rise (Shipboard Scientific Party, 2004). Grayscale scanning of OAE2 sediment has been used sporadically since 2001, but with relatively low-resolution data (Nederbragt et al., 2007; Eldrett et al., 2014; Meyers et al., 2001). Using new techniques in the present study, grayscale data over the entire 89-meter section of black shales at the Demerara Rise is measured on ODP core photographs at a ~600-micron resolution (the photograph resolution). This approach allows for remote research when the cores themselves cannot be accessed as in this case, where core photographs are accessible online but the cores are stored in Bremen, Germany.

Two unresolved discrepancies revolve around OAE2: the stratigraphic location of the Cenomanian-Turonian boundary within OAE2, and the duration of the event. These discrepancies have emerged most recently in biostratigraphic and chemostratigraphic research (Erbacher et al., 2005; Hardas and Mutterlose 2006; Jarvis et al., 2011; Meyers et al., 2012b; Li et al., 2017). The disparities in the previous research are likely due to different depositional environments among different locations. Differences in oceanography of the Atlantic, Pacific, and Tethys oceans, and other mechanisms, e.g. continental runoff, may influence changes in depositional features such as surface ocean productivity and terrigenous sediment influx that can alter sediment appearance and composition. Thus, microfossil stratigraphy and carbon isotope stratigraphy used as OAE2 chronological markers at different sites have yielded different results. Milankovitch cycles can be used to reconcile these discrepancies as they comprise a global signal that is consistent across the world.

In the present study, raw grayscale data extracted by the freeware *ImageJ* is correlated between two drill cores of Site 1261, and spliced together using the *Correlator* tool wherever there is a coring gap. Site 1261 is emphasized for this study as it contains few coring gaps, the longest interval of OAE2 (9.97 meters) of all Leg 207 sites, fair preservation of calcareous nannofossils, and a well-defined carbon isotope excursion (CIE). Using quantitative functions and procedures provided in *R* and *MATLAB*, stratigraphic frequencies related to Milankovitch cycles will be investigated for a 100-meter section of grayscale data that includes the laminated black shales and OAE2.

One limitation with this method is the inability to work directly with the drill cores, but high-resolution digital photographs are adequate for grayscale data. Other limitations include the presence of cracks and coring gaps, but can be adjusted by splicing data from both cores in *Correlator* and smoothing of grayscale scans.

Cretaceous Climate and the Global Carbon Cycle

The Cretaceous Period is part of the “greenhouse interval” of the Mesozoic Era which involved average surface temperatures greatly exceeding present day levels (Bralower et al., 2013). It also experienced periods of rapid warming and cooling, with a prominent warming event occurring across the Cenomanian and Turonian stages of the middle Cretaceous, peaking just before the Cenomanian-Turonian boundary at the onset of OAE2 (Figure 2; Friedrich et al., 2012).

At the peak of this warming event, average sea surface temperatures may have reached 32°C, with SST’s in the Southern Atlantic ranging from 26 to 30°C (Friedrich et al., 2012; Littler et al., 2011; Bralower et al., 2013). There were two main factors driving this increase in temperature. First, there were high levels of greenhouse gases in the atmosphere due to heightened volcanism (Larson, 1991a,b; Turgeon and Creaser, 2008), leading to CO_2 levels upwards of 1440 ppm (Friedrich et al., 2012; Scotese 2012; Wang et al., 2014). Second, shallow sills surrounding the North Atlantic might have prevented cool waters from entering the ocean basin (Poulsen et al., 2001; Friedrich et al., 2012). There was no ice at the poles, leading to high sea levels up to 250 meters higher than present (Miller et al. 2005; Müller et al., 2008; Hay, 2017). Epicontinental seas spanned every continent, including the Western Interior Seaway in North America.

Following the Coniacian-Santonian Oceanic Anoxic Event 3 (OAE3), temperatures gradually cooled to near modern-day levels by the end of the Cretaceous Period. This may have been due to the deepening of the Equatorial Atlantic Gateway as South America and Africa rifted apart. Deepening of the gateway possibly allowed southern Atlantic intermediate water to infiltrate northern Atlantic waters and yield cooler deep Atlantic waters at high latitudes between the Santonian and Campanian (Friedrich et al., 2012).

There was another extreme perturbation in the global carbon cycle, when $\delta^{13}C_{benthic}$ and $\delta^{13}C_{org}$ values temporarily deviated substantially in the North Atlantic Ocean. $\delta^{13}C_{benthic}$ excursions were on the magnitude of -3 parts per mil (ppm), whereas $\delta^{13}C_{org}$ varied by as much as +7 ppm (Friedrich et al., 2012, Erbacher et al., 2005). This is thought to have been caused by extended storage of organic carbon during the deposition of the middle Cretaceous black shales, changes in ocean circulation, and increased volcanic activity associated with large igneous provinces (Friedrich et al., 2012, Erbacher et al., 2001, Eldrett et al., 2014).

Geologic Setting and Lithology

The Demerara Rise is a submarine plateau on Paleozoic and Mesozoic rifted continental crust that represents a bathymetric extension of the continental shelf about 300 kilometers north of Suriname in South America (Shipboard Scientific Party, 2004; Basile et al., 2013). The plateau lies below sea level likely due to limited continental thinning and/or subsidence during the early Mesozoic (Greenroyd et al., 2008). It originated in the equatorial Atlantic Ocean just east of the southernmost edge of the Central Atlantic Ocean, which contains basaltic rock that dates back to 200 Ma as part of magmatism that created what is now known as the Central Atlantic Magmatic Province (CAMP) (Basile et al., 2013; Marzoli et al., 1999). Specifically, the equatorial Atlantic Ocean formed as a result of the South Atlantic Ocean's spreading axis propagating northward, and the Aptian-age rifting of Africa and South America (Basile et al., 2013, Shipboard Scientific Party, 2004). The western border of the Demerara Rise originated from a Jurassic divergent boundary, the northern border from an Early Cretaceous transform fault with a spreading axis in the Caribbean, and the eastern border from an Early Cretaceous divergent margin (Basile et al., 2013).

The rise covers about 380 km of coastline and is roughly 220 km from the shelf break to the northeastern-most section where the seafloor slopes down rapidly from 1000 meters to over 4000 m (Figure 2). It is considered to be one of the last sections in contact with West Africa just south of Dakar, Senegal (Shipboard Scientific Party, 2004).

Sediment accumulation on the Demerara Rise can be broken down into two stages (Gouyet et al., 1994). The first stage from 213 to 113 Ma is connected with the southward opening of the Central Atlantic that was located close to the Demerara Rise prior to initial rifting. Sedimentation occurred in a shallow marine, inner shelf environment during this time. The second stage from 113 Ma to present day is associated with the breakup of the French Guiana-Northeast Brazil margin from West Africa and the separation of the Demerara Rise. From this point, the depositional environment shifted from shallow to open marine (Greenroyd et al., 2008). Cenozoic sediment is only exposed near the top of the plateau around 700 meters below sea level (mbsl) as the sediment thins out and exposes Cretaceous deposits towards the escarpment at the northern and northeastern sections of the rise (Shipboard Scientific Party, 2004).

The target interval of the present study focuses on the finely laminated black shales deposited during the middle Cretaceous, from the Cenomanian to the Santonian (Figure 3; Shipboard Scientific Party 2004). The black shales are often referred to as “calcareous claystone” or “calcareous clay with nannofossils” according to Shipboard Scientific Party (2004). These black shales commonly contain a total organic carbon (TOC) content greater than 10 wt%, peaking at 25 wt% in the OAE2 interval (Nederbragt et al., 2007, Erbacher et al., 2005). The high TOC content during OAE2 and the rest of the black shale deposition leads it to be a principal source rock for oil production (Shipboard Scientific Party, 2004).

The shales contain several reoccurring geologic phenomena, including limestone stringers, ash beds, diagenetic calcite, and variations in carbonate content (Shipboard Scientific Party 2004). The differences in carbonate that make up most of the fine laminations are the cyclically recurring components of the Demerara Rise black shales that are used to investigate astronomical forcing of sediment deposition.

Biostratigraphy

Microfossils are present along the entire interval of the black shales, with a high concentration occurring within the OAE2 interval. These fossils include planktic foraminifera, radiolaria, and calcareous nannofossils. Planktic foraminifera in the black shale interval are relatively rare due to severe changes in surface water productivity and/or a shallow oxygen minimum zone (OMZ) inhibiting deep habitats for subsurface dwellers (Shipboard Scientific Party 2004, Nederbragt et al., 2007). Therefore, calcareous nannofossils are the primary index microfossils at the Demerara Rise.

Quadrum gartneri is a mobile planktonic photoautotroph that first occurred near the Cenomanian-Turonian boundary and last occurred during the Maastrichtian around 70.6 Ma (Burnett, 1998; Bown, 1998). *Quadrum* refers to its cubiform shape that does not have a central opening or diaphragm, and its elements join along sutures that extend to the edges of the cube. It is a member of the Haptophyte clade of algae that include coccolithophores (Manivit et al., 1977). It is one of two calcareous nannofossils, along with its sister taxon *Quadrum intermedium*, that is investigated for its first occurrence (FO) with respect to the stratigraphic location of the C-T boundary. *Q. gartneri* would thus be an associated event with the C-T boundary along with the ammonite *Watinoceras devonense*, which is the current biomarker for the Turonian Stage Global Stratotype Section and Point (GSSP) in the Bridge Creek Limestone Member at Pueblo, Colorado, USA (Kolonic et al., 2005; Kennedy et al., 2005).

Axopodorhabdus albianus is an elliptical calcareous nannofossil with a “3-tiered shield” that contains axial cross bars that protrude at the rim (Black, 1972). Also a member of the Haptophyte clade, it first occurred in the early Albian at ~108 Ma and last occurred in the late Cenomanian just before the C-T boundary (Burnett, 1998). Its last occurrence (LO) is the point of importance for this study.

These nannofossils can be traced to other localities around the world near the Cenomanian-Turonian boundary and then correlated with the CIE of OAE2. However, diachroneity of their occurrences with respect to the CIE cause them to be an inexact method of defining the C-T boundary, as discussed later in this study.

Milankovitch Cycles

Calibration of cyclicity within the black shales will be carried by exploiting Milankovitch cycles, which are caused by “metronomic” variations in the Earth’s movement with respect to the Sun over geologic time. There are three frequency bands of cycling with astronomical origins (Figure 4; Hays, et al., 1976; recent review in Hinnov, 2013).

(1) The precession index occurs with 19 and 23 kiloyear (kyr) cycles as the axially tilted Earth precesses in response to gravitational forces from the Moon and Sun with a period of 25.8 kyr. Precession causes the seasons to shift clockwise along the orbit with respect to the perihelion, the Earth's closest approach to the Sun. At the same time, the Earth's orbit experiences a general precession in longitude in the anti-clockwise direction. This reduces the time it takes for seasons to complete an orbital circuit, reducing and splitting precessional cycle periodicity to 19 and 23 kyr. (Hinnov, 2013).

(2) Obliquity varies in 41 kyr cycles, and refers to the axial tilt of the Earth. The tilt angle ranges from ~22° to 24.5°, and today is approximately 23.5°. A more severe tilt leads to increased solar radiation to the hemisphere facing the Sun and modifies the gradient of insolation as a function of latitude (Imbrie and Imbrie, 1979).

(3) Orbital eccentricity cycles act in 100 and 400 kyr periods (short and long eccentricity respectively) and is the variation in the eccentricity of the Earth's orbit around the Sun. Low eccentricity indicates a more circular orbit, whereas high eccentricity is a more eccentric orbit. The Earth's

orbital eccentricity has varied from 0.00005, to 0.0679, with an average eccentricity of 0.0019 (Laskar et al., 2004, 2011).

These astronomical cycles have an impact on the local solar radiation intercepting the Earth through time, and can be observed in the sedimentary record of climate such as elemental isotope and sedimentary records (Hinnov, 2013). Given that the astronomical cycles are a global phenomenon and that their periodicities change only slightly over time back to the Cretaceous (Laskar et al., 2004, 2011; Ma et al., 2017), Milankovitch cycles can be considered a worldwide proxy for correlating stratigraphy and for the study of the global paleoclimate system.

Previous Research

The first publication from ODP Leg 207 was an all-encompassing report of initial data and analyses (Shipboard Scientific Party, 2004). These data included lithology, magnetic susceptibility, biostratigraphy, and electrical resistivity, among other downhole logging data. Also included in the report are grayscale data, but at a much lower resolution than what is developed in the present study. Some key graphs in the preliminary data for Site 1261 appear to have errors, particularly in the correlation of core sections. There is also some uncertainty in the calculations of the meters below seafloor (mbsf) and meters composite depth (mcd) scales, where mcd is the placement of “coeval laterally continuous stratigraphic features into a common frame of reference by shifting the mbsf depth scales of individual cores to maximize the correlation between holes" (Shipboard Scientific Party, 2004). Nonetheless, this was the first major publication of data from Leg 207 and the initial standards for comparison in succeeding research.

Erbacher et al. (2005) identified a +6 per mil excursion of $\delta^{13}C_{org}$ at Sites 1258, 1260, and 1261, and established that the Cenomanian-Turonian boundary interval (CTBI) occurred near the end of the excursion at each site. This research referred to the CIE correlations of Tsikos et al. (2004), and added the CIE study from Site 1258 to the other correlated sites, including Pueblo, Colorado, Eastbourne, United Kingdom, and Tunisia (Figure 5). Erbacher et al. omitted biostratigraphic marker fossils from the correlations because only a few were found to occur in the Demerara Rise OAE2 interval. Point D in the carbon isotope curves is taken to correspond to the CTBI, and links the end of the CIE at each site. However, the CIE ends later at Eastbourne and Tunisia. The +6 per mil excursion at the Demerara Rise is also a substantially higher excursion than those at other sites, which are commonly on the order of +3 per mil. Erbacher et al. attests this to a high productivity regime due to upwelling conditions causing an increase in CO_2 uptake and a reduction in carbon isotope fractionation – a hypothesis first posited by Arthur et al. (1988) for the Cape Verde Basin off West Africa.

Adopting a 400 kyr duration for the OAE2 interval earlier established by Prokoph et al. (2001), Erbacher et al. estimated sedimentation rates of 1 cm/kyr, 0.25 cm/kyr, and 1.5 cm/kyr for sites 1258, 1260, and 1261, respectively. OAE2 data for Site 1259 were mostly omitted because the deepest drilled section in 1259 included only part of OAE2. This is thought to be due to an ongoing marine transgression and paleowater depth that was shallower than Site 1261. Erbacher et al. did not give specific reasons as to why the sedimentation rates vary so greatly from site to site, only saying that OAE2 was diachronous among the sites, and that Site 1260 was compacted.

Hardas and Mutterlose (2006) provided the first microfossil stratigraphy of Demerara Rise, and found several first occurrences and last occurrences of key calcareous nannofossil species at Sites 1258 through 1261. Preservation of the nannofossils ranged from good to very poor in the OAE2 interval, which was described as occurring between 627.99 and 637.0 mcd. Most of these nannofossils were considered in poor or moderate-poor condition. Hardas and Mutterlose do not propose any reasons for the poor preservation of these nannofossils, but this could be due to turbulent conditions and/or compaction over geologic time.

The FO and LO data were correlated with the carbon isotope records of Tsikos et al. (2004) and Erbacher et al. (2005) to identify the Cenomanian-Turonian boundary with respect to two nannofossil events: the FO of *Q. gartneri*, and the LO of *A. albianus* (Figures 6 and 7). The C-T boundary is positioned slightly earlier than the estimate of Tsikos et al., (2004), closer to the middle of the CIE. They also propose that the C-T boundary is located at the FO of another nannofossil, *Q. intermedium*.

However, the FO of *Q. gartneri* at Site 1258 occurs much earlier than at 1260 and 1261. Hardas and Mutterlose cite potentially undiscovered earlier occurrences of *Q. gartneri* and/or diachroneity to explain this inconsistency, and this may be part of the reason why the Demerara Rise is not included in their site correlation figure. Additionally, there is uncertainty with the LO of *A. albianus* in Site 1260 and is not correlated with the Bonarelli Level at Gubbio, Italy (no trace of *A. albianus*) nor the Tarfaya Basin in Morocco (offset CIE peaks and diagenetic overprinting) (Hardas and Mutterlose, 2006; Tsikos et al., 2004).

Nederbragt et al. (2007) introduced cyclostratigraphic records of Leg 207 together with an analysis of core sediment composition and facies. Included in this report is information on the paleogeography and geological setting of Demerara Rise and a hypothesis of plausible ocean circulation behavior during the mid-Cretaceous. Nederbragt et al. adopted Erbacher et al. (2005)'s synopsis that significant biostratigraphic marker species were scarce, and that assemblage diversity was low due to a shallow oxygen minimum zone.

The lithology and sediment texture of the entire mid-Cretaceous for each drilled core in Leg 207 were presented. Key lithologies were identified as organic-rich intervals and carbonate-rich intervals. Organic-rich intervals in the darker core sections included microfossils such as planktonic foraminifers, fecal pellets, and high amounts of phosphate stringers and nodules. Large specimens occur infrequently, and there is little discussion of the calcareous nannofossils that had been examined by Hardas and Mutterlose (2006).

Carbonate-rich intervals include pelagic beds and packstones within the carbonate-rich beds that are commonly laminated. Carbonate content is 50 to 90 wt% except within the OAE2 interval, where carbonate is <50 wt% and clays predominate. The carbonate-rich intervals are heavily bioturbated at the deeper Sites 1257 and 1258, and less so at Sites 1260 and 1261. Microfossils, mostly planktic foraminifera, are more sporadic and/or poorly preserved in packstones. Laminations in these intervals are often parallel and continuous.

Nederbragt et al. computed power spectra on stratigraphic series of sediment color measurements (2.5 cm spacing) to search for Milankovitch cycles in stratigraphy thickness. Most of the power spectra produced split peaks that were attributed to changes in sedimentation rate and varying degrees of compaction. Identification of cycle patterns sometimes fell on visual interpretation where power spectra were exceptionally poor. Nevertheless, power spectra and bandpass filters identified bundling of five 20 kyr precession cycles within one short (~100 kyr) eccentricity cycle, and obliquity cycles were calculated to have a 38.8 kyr periodicity. Cycle thicknesses and durations varied among the sites. Adequate power spectra were limited due to only a “very few rhythmically bedded geological sections” (Nederbragt et al 2007). The present study will improve on these data with high resolution (0.6 mm) grayscale scans from the digital ODP photo images that can detect color changes at the millimeter scale.

Meyers et al. (2012b), significantly improved Demerara Rise cyclostratigraphy with analysis of high-resolution (1.27 cm spacing) Formation MicroScanner (FMS) well logging data. Meyers et al. used Evolutive Harmonic Analysis (EHA) (Meyers et al., 2001) and the Average Spectral Misfit (ASM) method (Meyers and Sageman, 2007) to test the presence of astronomical forcing on OAE2 sedimentation.

Using these two tools along with power spectral analysis of the 40-meter section of FMS data from Site 1261B, obliquity was discovered to be the dominant cycle for the accumulation of organic matter during OAE2. Meyers et al. proposed that the strong obliquity signal implicates a high-latitude climate influence in which the CO_2 impact on temperature is more pronounced and that volcanism warmed intermediate ocean waters, causing a change in ocean circulation leading to de-stratification. Estimation of sedimentation rates for Site 1261B were conducted for two 6-meter intervals within the 89 m long black shale sequence: one within OAE2, and the other above OAE2 in the early Turonian.

Currently the numerical age of the C-T boundary is 93.9 ± 0.1 Ma, from joint astrochronologic-radioisotopic calibration by Meyers et al. (2012a). For their Demerara Rise study, Meyers et al. (2012b) follow Kolonic et al. (2005) that the C-T boundary is at the FO of *Q. gartneri*. However, as discussed, *Q. gartneri* should not be used a global C-T biomarker due to an apparent diachroneity arising from differences in depositional environments and fossil preservation. Meyers et al. also hypothesized that dense high-latitude water displaced nutrient-rich anoxic deep water in the North Atlantic and created an episode of increased organic activity that lasted for 700 to 800 kyr. This is significantly longer than the initial estimates of OAE2 being a ~400 kyr event.

Li et al. (2017) analyzed the OAE2 interval in core drilled in southern Tibet. Spectral analyses computed on detrended magnetic susceptibility data found a dual-mode for short orbital eccentricity (95 and 125 kyr) and precession (18 and 23 kyr). These astronomical constraints were used to define time durations within OAE2, which was broken down into five “stages” (Figure 8). Short orbital eccentricity cycles were identified in each stage and a total duration of the CIE associated with OAE2 was estimated to be 820 kyr (Li et al., 2017).

This is also substantially longer than previous estimates for the duration of OAE2, and follows the trend of recent studies concluding that OAE2 encompassed more time than previously expected (Meyers et al., 2012b, Li et al., 2017). The present study, as will be demonstrated, is consistent with this expectation.

DATA

To collect grayscale data, boxed core photographs from the entire black shale interval in Leg 207 were downloaded from the ODP website (Figure 9). A tool known as *ImageJ* is then used to extract grayscale values by positioning a line created by the software centered along each core section (Appendix A). Both RGB and grayscale are measured for each pixel falling on the line along the core sections. *ImageJ* allows for high-resolution pixel color and grayscale data to be captured, creating ~2550 points per 1.5m core section, an average of one point every ~590 microns. The data are assembled in Microsoft Excel and converted to the format necessary for loading into *Correlator*.

Correlator is the splicing tool used when there is a gap in the core in one drill hole that can be filled by a second nearby core at the same depth (Appendix B). *Correlator* utilizes two techniques – correlation and splicing. Correlation is performed by finding similarities in grayscale patterns such as peaks and troughs, and shifting one core with respect to another to align these patterns (Figure 10). This modifies core intervals with respect to original mbsf depth and creates a new composite depth scale (here kmcd = Karoly modified composite depth), as original core depth may be incorrect due to improper coring, discontinuities, and compaction.

Once the grayscale data have been correlated, gaps can be filled by splicing data from one core into the other. When the splicing is completed, the resulting composite record can be exported from *Correlator* back into Excel (Figure 11). This composite grayscale record can be correlated to the carbon isotopes and biostratigraphy cited above, and analyzed for Milankovitch cycles.

METHODS

Spectral Analysis

The composite grayscale record will be analyzed using multiple taper power spectral analysis (Thomson, 1982, 2009; Kodama and Hinnov, 2015). The power spectrum of the record is expected to reveal spectral peaks at specific wavelengths indicative of Milankovitch scale cyclicity (similar to the results of the FMS study by Meyers et al., 2012b). The power spectrum distributes the variance of a time series as a function of frequency (Figure 12) and is determined with the Fourier transform and averaged for statistics (Percival and Walden, 1993). Discrete, truncated (i.e., with a beginning and an end) time series, such as the grayscale scan series in this study, benefit from tapering the beginning and ends of the series to suppress leakage of variance into adjacent frequencies, and increase the degrees of freedom of the estimated power. Traditionally, single tapers such as the Hann taper have served this purpose (Figure 13a; recent review in Kodama and Hinnov, 2015), but today multiple tapers can be applied to time series, notably the discrete prolate Slepian sequences (DPSS's) (Figure 13b; Thomson, 1982). A harmonic line test was developed in which signal-to-noise ratios with F-distributions are constructed from the multitapered spectra (Thomson, 1982). This test is applied as a prerequisite step for the ASM procedure discussed below.

The evolutionary Fast-Fourier Transform (FFT) Spectrogram (Kodama and Hinnov, 2015) will be implemented to determine the relative strengths of frequencies as a function of sediment core depth. The FFT spectrogram uses the *MATLAB* script evofft.m (Appendix C) to create a moving time window given a step increment. An unsmoothed (untapered) periodogram is calculated for each window which is normalized to itself, and tracks the “evolution” of the primary frequency components of each window.

The FFT spectrogram is similar to the amplitude spectrogram in Evolutive Harmonic Analysis (EHA) (Meyers et al., 2001). Either technique can be used to identify changes in sedimentation rate when Milankovitch scale cyclicity is indicated in a sedimentary section, and can reveal any transitions from one astronomical forcing parameter to another (e.g., a change from dominant obliquity forcing to dominant precession forcing). Here the FFT spectrogram is used in order to take advantage of the expanded graphics options in MATLAB.

Average Spectral Misfit Method

The average spectral misfit (ASM) method "seeks to identify the sedimentation rate that minimizes the misfit between the observed frequencies and predicted orbital components” (Meyers and Sageman, 2007) (Figure 14). The ASM metric represents the average distance between observed and theoretical Milankovitch, or “astronomical target” frequencies. For this study, the observed frequencies are the set of significant lines determined for the data spectrum from application of the harmonic line F-ratio test described above. The astronomical target frequencies at ~94 Ma are according to the Supplemental Information of Meyers et al. (2012b) that combine results from the astronomical model of Lasker et al. (2004, 2011) and Berger et al. (1992) (Appendix C). The target frequencies are: 1/(405.47 kyr) (long orbital eccentricity), 1/(126.98 kyr) and 1/(96.91 kyr) (short orbital eccentricity), 1/(37.66 kyr) (obliquity), and 1/(22.42 kyr) and 1/(18.33 kyr) (precession index). When ASM is low or zero, the observed frequencies are nearly identical or identical to the astronomical target frequencies.

A range of "test" sedimentation rates are used to convert the stratigraphic data power spectrum (with frequencies in cycles/meter) into time series power spectra (with frequencies in cycles/kyr), from which the ASM metric is calculated. For each tested sedimentation rate, a Monte Carlo procedure repeatedly (e.g., 1000 times) randomizes the observed frequencies, to calculate a large set of ASM metric values. If only a few of the Monte Carlo randomizations produce ASM metric values at or lower than the observed ASM metric value, the null hypothesis of "no astronomical forcing" can be rejected. The critical rejection level is indicated by a horizontal dashed line in the ASM output, and equals the inverse of the number of sedimentation rates being tested (Figure 15).

The composite grayscale record will be imported into *R* to apply the ASM method as provided in the *Astrochron* package (Meyers, 2014) and determine the most likely sedimentation rate(s) for the record and likelihood for Milankovitch. This will be done for the entire 89 m long black shale interval, and separately for the OAE2 interval (as defined by the CIE). The results will allow a chronology to be assigned to OAE2, and to assess differences in sedimentation rates in OAE2 compared to the rest of the black shale interval.

Pre-processing

A composite grayscale graph for the black shale interval created in *Correlator* displayed continuous core throughout the interval with the exception of two gaps located between 600.39 and 601.02 kmcd (see below), and 619.2 and 621.4 kmcd (Figure 11). The composite dictated that Core A is not adjusted depth-wise and thus remains consistent with mbsf, and that Core B is shifted when appropriate to correlate grayscale data between the two drill cores and to patch as many gaps as possible that appear in Core A. This depth composite is therefore referred to as "Karoly meters composite depth", or "kmcd". Core A is prioritized throughout the interval due to greater variability in grayscale peaks and troughs than Core B to assist with Milankovitch identification. Core A is also emphasized in order to minimize shifting of Core B to Core A.

Splice points from Core B into Core A were based on closest resemblance in grayscale behavior, such as the aforementioned peaks and troughs. Appropriate shifting was performed manually by matching grayscale peaks and verified using preliminary data from Scientific Shipboard Party 2004.

In preparing the grayscale data for *MATLAB* and *R*, the composite grayscale record was cleaned by removing all depth values with a gap (in drill cores, gaps, i.e. absences of cored material are monitored and measured the cored sections). Slight differences in Image-J data collection when defining pixels per meter created minute variations in sampling rate throughout the interval, but commonly ranged from 580 to 600 microns. These differences most commonly occurred in core sections that did not completely fill the 1.5 m long core columns. The estimated median sample rate of 590 microns was confirmed by MATLAB and subsequently used to produce an interpolated grayscale record with a uniform sampling step of Δd=0.590 mm.

Estimation and removal of anomalously high amplitude, irregular low frequency trends, known as “prewhitening”, assists spectral analysis to focus on frequencies of interest. Using weighted moving averages (LOESS="LOcal regrESSion"), these trends can be estimated and removed to minimize interference with the target spectrum (Kodama and Hinnov, 2015). For the uniformly sampled, cleaned grayscale record, pre-whitening by removal of a 10 m and 20 m windowed LOESS curve was undertaken (Figure 16; Appendix D).

RESULTS

Spectral Analysis

A 2π MTM power spectrum of the 89.38-m pre-whitened grayscale series shows prominent spectral peaks that according to ASM results (see next section), can be attributed to Milankovitch forcing from precession, obliquity, short eccentricity, and long eccentricity (Figure 17). Long and short eccentricity signal strength were nearly the same and are the dominant signal in the power spectrum. A sedimentation rate of 1.48 cm/kyr was estimated for a post-OAE2 interval in the Formation MicroScanner well log for Hole 1261B from 609.8 to 615.8 mbsf (=611.44 to 617.44 kmcd) by Meyers et al. (2012b). This suggests that the strong spectral peak at 6.18 m could be the 405 kyr “long” eccentricity cycle, i.e., 618 cm / (1.48 cm/ kyr) = 417.57 kyr. This would calibrate the spectral peaks at 1.65 m and 1.0 m to the “short” eccentricity, the peaks from 0.65 to 0.41 m to the obliquity, and peaks from 0.34 m to 0.24 m to the precession.

The evolutionary FFT spectrogram for grayscale series supports the MTM power spectrum representation of an interval dominated by eccentricity power (Figure 18). Long eccentricity power dominated the black shales at two intervals: from the start (653.51 to 622 kmcd), and from 566 kmcd to the top of the scan, which includes the transition into lighter claystone and chalk. For these two intervals, short eccentricity power virtually disappears. On the other hand, sections where short eccentricity power is dominant, long eccentricity power vanishes. This interchange between dominant long and short eccentricity is expected, according to the theoretical eccentricity plot by Laskar et al. (2004) (see below). Obliquity power also fades significantly in power during periods when long eccentricity is the dominating cycle.

Sedimentation Rates and OAE2 Interval

Using the *astrochron R* package (Meyers, 2014), ASM was conducted on the grayscale record to determine if Milankovitch cycles are present and whether varying sedimentation rates affect the 89.38 m long black shale interval. The grayscale scan was separated into 10-meter intervals, except for the top and bottom of the black shale interval (5.87 m and 3.51 m, respectively), with the goal of attaining a <1% H_o-Significance Level. A 1% H_o-Significance Level indicates that there is a 1% probability for the ASM generated sedimentation rate to have been derived by chance in fitting closely to the astronomical target (Meyers and Sageman, 2007). The 10-m grayscale intervals were interpolated to a uniform 590-micron sampling rate, and multi-taper harmonic line F-testing was performed to estimate statistically significant line frequencies (Kodama and Hinnov, 2015).

The aforementioned Milankovitch frequencies at the C-T boundary established by Meyers et al. (2012b) were set as the target frequencies. Significant line frequencies in the grayscale scan were assessed at the 90% significance level and a frequency of ≤ 5 cycles per meter were identified according to the MTM power spectra produced in *R* (Appendix E). The Rayleigh frequency, the frequency resolution was determined for each interval based on its precise length in m; the Nyquist frequency was manually reduced to 10, the frequency range with most of the power. 100 sedimentation rates from 0.1 cm/kyr to 5 cm/kyr were tested for each interval. 1000 Monte Carlo simulations, which generate randomly distributed spectra with the same Rayleigh resolution, were run to determine the statistical significance of each ASM test.

ASM revealed varying sedimentation rates throughout the entire 89.38-m grayscale record from 564.13 to 653.51 kmcd. The start and end points for the black shale interval are easily recognizable given transition points from shale to other rock (e.g. quartz sandstone) on the imagery provided by the ODP. Specifics on each section are displayed in Figure 19 and Table 1. Sedimentation was as slow as 1.029 cm/kyr in the 620 to 630 kmcd section that immediately follows the OAE2 event, and as high as 2.269 cm/kyr during the middle Turonian period.

The sedimentation rate for the 9.97-m long OAE2 interval between 629.97 and 639.94 kmcd was 1.071 cm/kyr at a 1% H_o-Significance Level. This core interval was defined based on carbon isotope values from Erbacher et al. (2005) and equates to 931 kyr for OAE2.

Using the sedimentation rates for the analyzed intervals, the duration for the entire 89.38 m black shale given an average of 1.384 cm/kyr is approximately 6450 kyr, likely spanning the late Cenomanian to the late Coniacian. This is roughly 4.6 million years shorter than the estimate posited by the Shipboard Scientific Party (2004) who extended the laminated black shale interval to the end of the Santonian and nannofossil zone CC14 at 83.6 Ma. This has proven to be incorrect, because the top of nannozone CC14 is most likely confined to the Coniacian (see Figure 26.7 in Ogg and Hinnov, 2012).

Calibration of the 2π MTM power spectrum by ASM transitions the spectrum in the distance domain from Figure 17 into a new power spectrum in the time domain (Figure 20). The signal cyclicity (now in kyr) is based on the average sedimentation rate of 1.384 cm/kyr obtained by ASM testing. After converting to the time domain, proposed Milankovitch peaks based on this power spectrum are: 446.5 kyr long eccentricity, 100.65 kyr short eccentricity, 46.97 kyr obliquity, and 21.49 kyr precession (Table 2).

Theoretical Orbital Eccentricity

To support the conclusion for the presence of strong orbital eccentricity cycles in the black shales, an equivalent FFT spectrogram of the La2004 theoretical orbital eccentricity (Laskar et al., 2004) from 95 Ma to 89 Ma was used as a basis of comparison (Figure 21; Appendix E). Three similarities with the grayscale spectrogram (Figure 18) are evident. Firstly, the repeated exchange in power between long and short eccentricity is evident through the spectrogram. Secondly, long eccentricity power appears at the appropriate time intervals. The C-T boundary at 93.9 Ma is dominated by the long eccentricity, and this correlates to a similar pattern the grayscale spectrogram where the C-T boundary is theorized to occur at 637 kmcd (Meyers et al. (2012a,b). Lastly, the braided pattern in the evolution of the short eccentricity spectrum in the grayscale scan emulates a similar pattern observed in the theoretical orbital eccentricity for the same time period.

DISCUSSION

Cenomanian-Turonian Boundary Discrepancy

As noted, there is considerable uncertainty with the first occurrence of *Q. gartneri*, especially at Leg 207. Hardas and Mutterlose (2006) found that the FO of *Q. gartneri* lies at similar depths between Site 1260 and 1261, but appeared significantly earlier at Site 1258 and could not be defined at all in Site 1259 due to the cored interval beginning at shallower depths.

Figure 22 depicts FO and LO data for *Q. gartneri* and *A. albianus*, respectively, superimposed on Site 1261 carbon isotope data (Hardas and Mutterlose, 2006; Erbacher et al., 2005). This is correlated with chemostratigraphy at Pueblo, Colorado, USA, and Eastbourne, UK by Tsikos et al. (2004). The Bridge Creek Limestone Member at the Pueblo site is the location of the GSSP for the Cenomanian-Turonian boundary which is currently defined by the FO of the ammonite *Watinoceras devonense* (Kennedy et al., 2005).

The FO of *Q. gartneri* is also used as a biomarker for the C-T boundary as an "associated event" (Kolonic et al., 2005), where the C-T boundary occurs at or below the FO of *Q. gartneri* depending on the site, similar to Figure 6 by Hardas and Mutterlose (2006). However, the C-T boundary appears to occur simultaneously with the FO of *Q.*

gartneri in Meyers et al. (2012a,b). Kolonic et al. (2005) also indicate that the FO of *Q. gartneri* marks the end of the OAE2 interval at Pueblo, CO and Eastbourne, UK, while it occurs towards the middle of OAE2 at the Demerara Rise in Figure 22.

Figure 22 also shows that nannofossil data from Hardas and Mutterlose (2006) places *Q. gartneri* closer to point C on the carbon isotope curve before the C-T boundary, whereas at Pueblo *Q. gartneri* FO occurs after point D, towards the end of the CIE and after the C-T boundary (Tsikos et al., 2004). This is consistent with Nederbragt and Fiorentino (1999) who suggest that the FO of *Q. gartneri* is before the start of the Turonian at Oued Mellegue, Tunisia. At Site 1258, FO of *Q. gartneri* occurs before point C, even lower than at Site 1261. Given the mcd scale in Erbacher et al. (2005), the differences in these FO's and the FO at Pueblo could be as much as four meters, or ~400 kyr using the sedimentation rate found for the OAE2 interval (see above). Similarly, the LO of *A. albianus* occurs below point B at Sites 1258 and 1261 at the Demerara Rise, but after point C at other localities such as Pueblo, CO, Eastbourne, UK, and the Tarfaya Basin (Tsikos et al., 2004; Hardas and Mutterlose, 2006). In sum, the FO of *Q. gartneri* is not only inconsistent among locations from different parts of the world, but also among sites at the Demerara Rise. Due to apparent diachroneity of calcareous nannofossil occurrences and differences in environment depending on location, *Q. gartneri* should not be used as an associated event with both excursion points during OAE2 and the C-T boundary.

The inconsistency in the CIE is also demonstrated by Figure 22. While more consistent than the biostratigraphy for the C-T boundary, carbon isotope records feature differences in magnitude and behavior. The CIE at Site 1261 is +7 ppm, but only +4 ppm at Pueblo, Colorado and +2.5 ppm at Eastbourne, UK. Point B is represented by a very brief return to near-normal carbon isotope levels at Site 1261 and Eastbourne, UK, but this point is non-existent at Pueblo, Colorado. Point D is uniformly marked by a peak excursion point in most sites, but at Eastbourne, UK, the it is negligible. Furthermore, each location varies in the amount of time it takes for carbon isotope values to return to normal background levels after OAE2.

Alternatively, the end of a long eccentricity cycle at ~93.9 Ma – together with minimum amplitudes in all of the astronomical parameters – can be associated with the C-T boundary, and serve as a basis for global cyclostratigraphic correlation of the C-T boundary (Figure 23).

OAE2 and the Laminated Black Shale Interval

The 1.071 cm/kyr estimated sedimentation rate for the OAE2 interval is marginally slower than the 1.14 cm/kyr rate found by Meyers et al. (2012b), but is significantly slower than the ~1.5 cm/kyr estimate first theorized by Erbacher et al. (2005). However, Erbacher et al. defined a 1.5 cm/kyr sedimentation rate for Site 1261 given the length of the OAE2 interval recovered and assuming a 400 kyr duration for the CIE, based on a chronology of “short-termed sea level, carbon cycle, and climate variations during the Cenomanian-Turonian Boundary Event in NW Europe” (Erbacher et al., 2005; Voigt et al., 2005). Just ~80 km northeast, the same data suggest that Site 1260 had a sedimentation rate of 0.25 cm/kyr for the OAE2 interval. Erbacher et al. (2005) later proposed that the overall sedimentation rate of the Cenomanian-Coniacian laminated black shale interval was 0.85 cm/kyr, which is the opposite trend of the sedimentation rates found in this study where the OAE2 interval is one of the slower sections of sediment deposition.

The 931 kyr duration for OAE2 would currently be the longest estimate for this event given a previous high of 820 ± 25 kyr (Li et al., 2017). This continues the trend of increasing time intervals for OAE2, beginning with ~400 kyr in Erbacher et al. (2005) and evolving to 700-800 kyr (Meyers et al., 2012b), 710 ± 170 kyr (Eldrett et al., 2015), and most recently the Li et al. (2017) estimate of 820 ± 25 kyr. However, Meyers et al. (2012b) use 626.47 to 637 mcd to delineate OAE2 based on carbon isotopes from Erbacher et al. (2005). Given this length of 10.53 m, and their estimated OAE2 sedimentation rate of 1.14 cm/kyr, this would yield an OAE2 of ~924 kyr – only 7 kyr difference from the 931 kyr estimate from this paper. Meyers et al. (2012b) do not mention a change in sedimentation rate during the OAE2 interval that would justify the 700 to 800 kyr estimate. Nonetheless, estimation for this interval remains difficult due not only to possible hiatuses, but also due to its anomalously high organic and clay composition and a high susceptibility to compaction.

On the other hand, the ~6450 kyr duration for the entire black shale section is much lower than previous intervals established of 11 myr (Shipboard Scientific Party, 2004) and 10.1 myr (Ogg and Hinnov, 2012). However, this high-resolution grayscale scan is supported by the theoretical eccentricity spectrogram that depicts three dominant long eccentricity intervals in the ~6 myr time window of 95 to 89 Ma. Extending the theoretical orbital eccentricity spectrogram to 10 myr between 95 and 85 Ma shows five to six sections dominated by long eccentricity (Figure 24). This would not be consistent with the black shale spectrogram from Site 1261.

The Evidence for Milankovitch Cycles

The power spectrum and evolutionary spectrogram of the grayscale scan clearly reveal Milankovitch scale cyclicity throughout the black shale interval and OAE2. This can also be seen in the presumed short eccentricity meter-scale cyclicity of the grayscale scan. These black shale cycles are dominated by eccentricity; evidence for obliquity cycles also exists but is weaker.

Plausible obliquity and precession periodicities of 36.17 and 21.49 kyr, respectively, are shorter than calculated for the present-day. This may be attributed to increased speed in Earth’s rotation and shorter length of day of ~23 hours in the Early Cretaceous (Laskar et al., 2004; Hinnov and Hilgen, 2012). Further refinement is necessary: cycle thicknesses change within each 10m section tested due to variable sedimentation rates.

These rates can be used to convert the grayscale scan from the stratigraphic domain to the time domain. This should significantly improve the alignment of the obliquity and precession band cycles.

CONCLUSIONS

Using Milankovitch cycles as a global signal should reconcile differences in biostratigraphic and chemostratigraphic studies for not only the C-T boundary, but also other geologic events in which there is disagreement in the time domain. The FO of *Q. gartneri* has proven to be unreliable to establish the C-T boundary, while carbon isotopes are more consistent in behavior but still vary among locations.

This study strives to provide a cornerstone reference for future Milankovitch studies of OAE2 and other geologic events, especially where they exploit the global consistency of Milankovitch cycles. If future studies concur that the current highly resolved C-T boundary occurs simultaneously with the end of a short orbital eccentricity cycle (as proposed by Mitchell et al., 2008 and Lanci et al. 2010; see Figure 23) then it can be used globally as a proxy for both OAE2 and the C-T boundary considering the consistency and synchroneity of Milankovitch cyclicity around the world.

Future work on grayscale scans of the Demerara Rise cores can further support the results presented in this paper. Compiling a composite grayscale record of Sites 1258 and 1260 can provide an intra-expedition basis for correlating to Site 1261. Performing gap filling techniques in *MATLAB* can provide a complete, quasi-continuous grayscale composite series, as well as refine sedimentation rates, the time scale, and power spectra.

Further compartmentalizing the black shales into smaller segments (e.g. five meters) may be necessary as the FFT spectrogram indicates that sedimentation rates may vary on a scale less than the 10-meter interval that was used to conduct ASM testing in this paper. Lastly, tuning is necessary to better resolve obliquity and precession frequencies in power spectra and to produce a more accurate signal. Red noise hypothesis testing can then be employed on the “tuned” power spectra to determine which spectral peaks are statistically significant.

TABLES

Table 1: Sedimentation rate and subsequent time duration by interval tested using ASM. Included are core boxes used in each interval according to the Correlator composite, and the number of significant frequencies at or less than five cycles per meter that surpassed the 90% MTM harmonic F-test significance level. See Figure 19 for further results. R commands for ASM are in Appendix C. The sum of all intervals is 7383.65 kyr.

Depths (kmcd)	**Core boxes included in section**	**Sedimentation Rate (cm/kyr)**	**Duration**	**Significant Frequencies (≤5 cycles/m)**
554.2 to 564.12	40A, 5B, 41A	1.072	925.37 kyr	10
564.13 to 570	41A	1.254	468.10 kyr	7
570 to 580	41A, 42A	1.205	829.88 kyr	9
580 to 590	42A, 43A, 8B	1.720	581.40 kyr	12
590 to 600	8B, 44A	1.159	862.81 kyr	10
600 to 610	9B, 45A	1.654	604.59 kyr	9
610 to 620	10B, 46A	2.269	440.72 kyr	12
620 to 630	46A, 47A	1.029	971.82 kyr	9
630 to 640	47A, 12B, 48A, 13B	1.071	933.71 kyr	6
640 to 650	48A, 13B, 49A	2.015	496.28 kyr	13
650 to 653.51	14B, 50A	1.305	268.97 kyr	2

Table 2: Table of significant peaks identified in power spectrum. Stratigraphic domain is rounded to the nearest hundredth meter. Average sedimentation rate of 1.384 cm/kyr is assumed for the entire 89.38 m black shale interval. Plausible orbital eccentricity, obliquity and precession frequencies are noted at the right. See Figure 20.

Thickness (meters per cycle)	**Stratigraphic Frequency (cycles/m)**	**Periodicity (kyr)**	**Power**	**Notes**
6.18m	0.17	446.50 kyr	9.84 E4	Long eccentricity
3.03m	0.33	219.12 kyr	5.31 E4	?
1.65m	0.61	118.89 kyr	5.29 E4	?
1.39m	0.72	100.65 kyr	9.99 E4	Short eccentricity
1.20m	0.83	86.62 kyr	4.35 E4	?
1.00m	1.00	72.10 kyr	3.09 E4	?
0.75m	1.33	54.25 kyr	3.03 E4	Obliquity 1
0.65m	1.54	46.97 kyr	3.08 E4	Obliquity 2
0.53m	1.89	38.51 kyr	1.54 E4	?
0.50m	2.00	36.17 kyr	1.43 E4	Obliquity 3
0.41m	2.44	30.04 kyr	1.20 E4	?
0.34m	2.94	24.51 kyr	9.70 E3	Precession 1
0.30m	3.33	21.49 kyr	1.07 E4	Precession 2
0.24m	4.17	17.46 kyr	5.88 E3	Precession 3

FIGURES

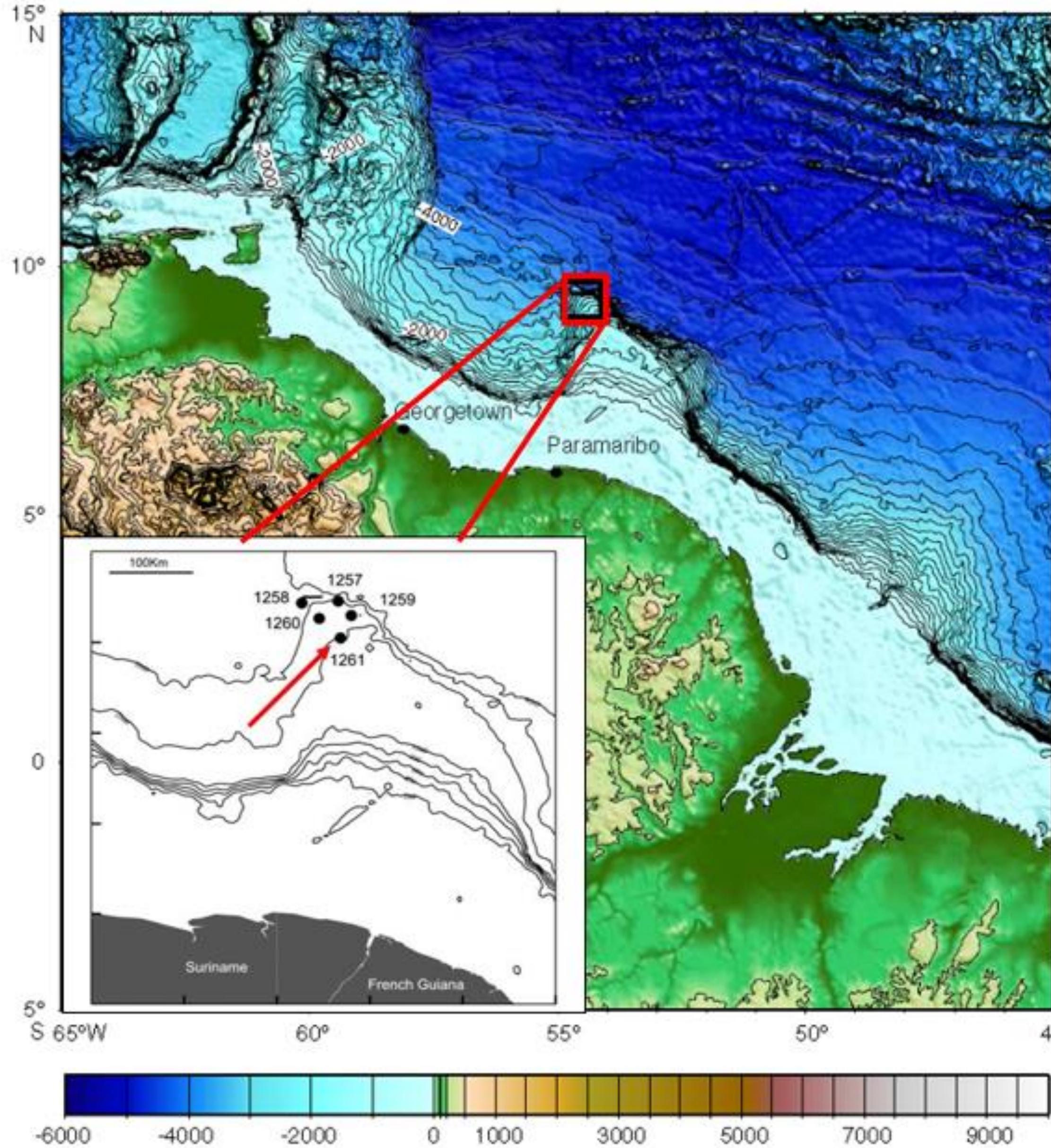

Figure 1: Location of ODP Leg 207 (red rectangle) ~280 km off shore of Paramaribo, Suriname. From Shipboard Scientific Party (2004). Insert of Leg 207 Site locations from Hardas and Mutterlose (2006). Red arrow points to Site 1261, the focal site of this paper.

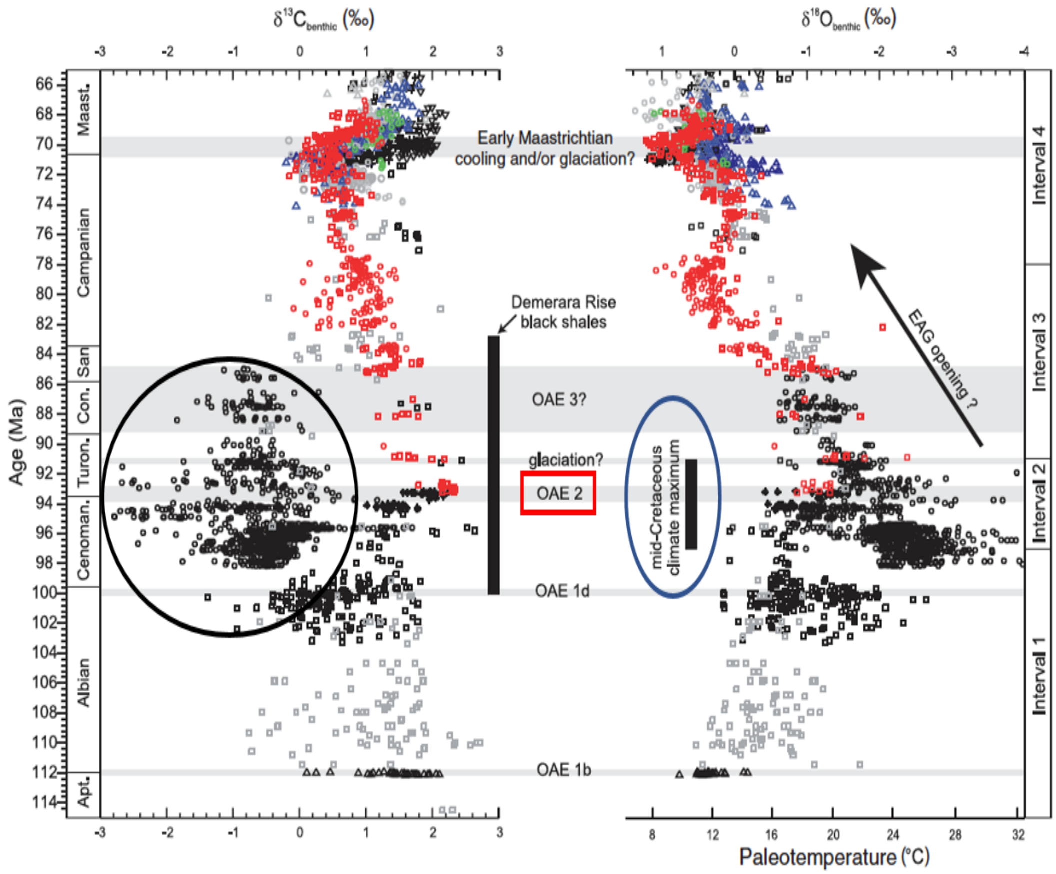

Figure 2: Oxygen and carbon isotopes of benthic foraminifera from 115 Ma to 65 Ma. OAE2 occurs at the narrow interval at 94 Ma. Black points indicate data from the Atlantic Ocean. Circled in black is a negative $\delta^{13}C$ excursion, particularly noticeable at the onset of OAE2, thought to indicate anomalously "old" water masses. The blue circle highlights the climate maximum of the mid-Cretaceous that encompasses OAE2 and the CIE. Examples of the CIE are shown in Figures 5, 6, 7, and 8. The Demerara Rise black shales span the Cenomanian-Coniacian, and thought to represent an ~11 myr duration. Modified from Friedrich et al. (2012).

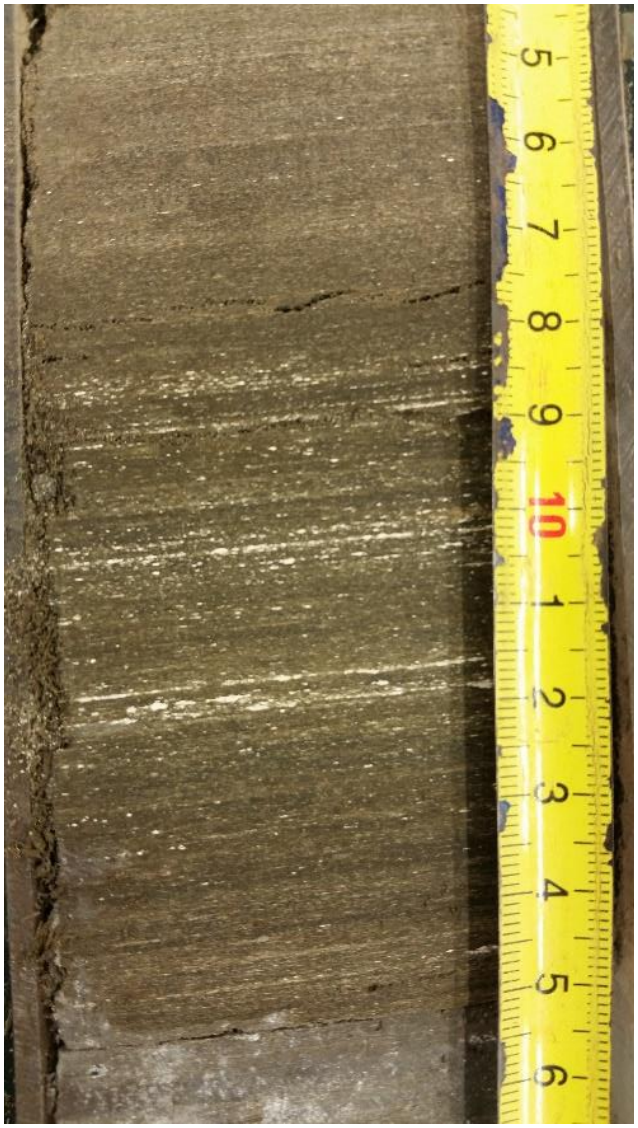

Figure 3: High-resolution photo of Site 1261, Core 13B, Section 2, 638.77 to 638.93 kmcd. Note millimeter scale laminations. Lighter color lithologies suggest higher carbonate content. Near-white laminations indicate high organic activity (foraminiferal hash). Photo taken by M'bark Baddouh.

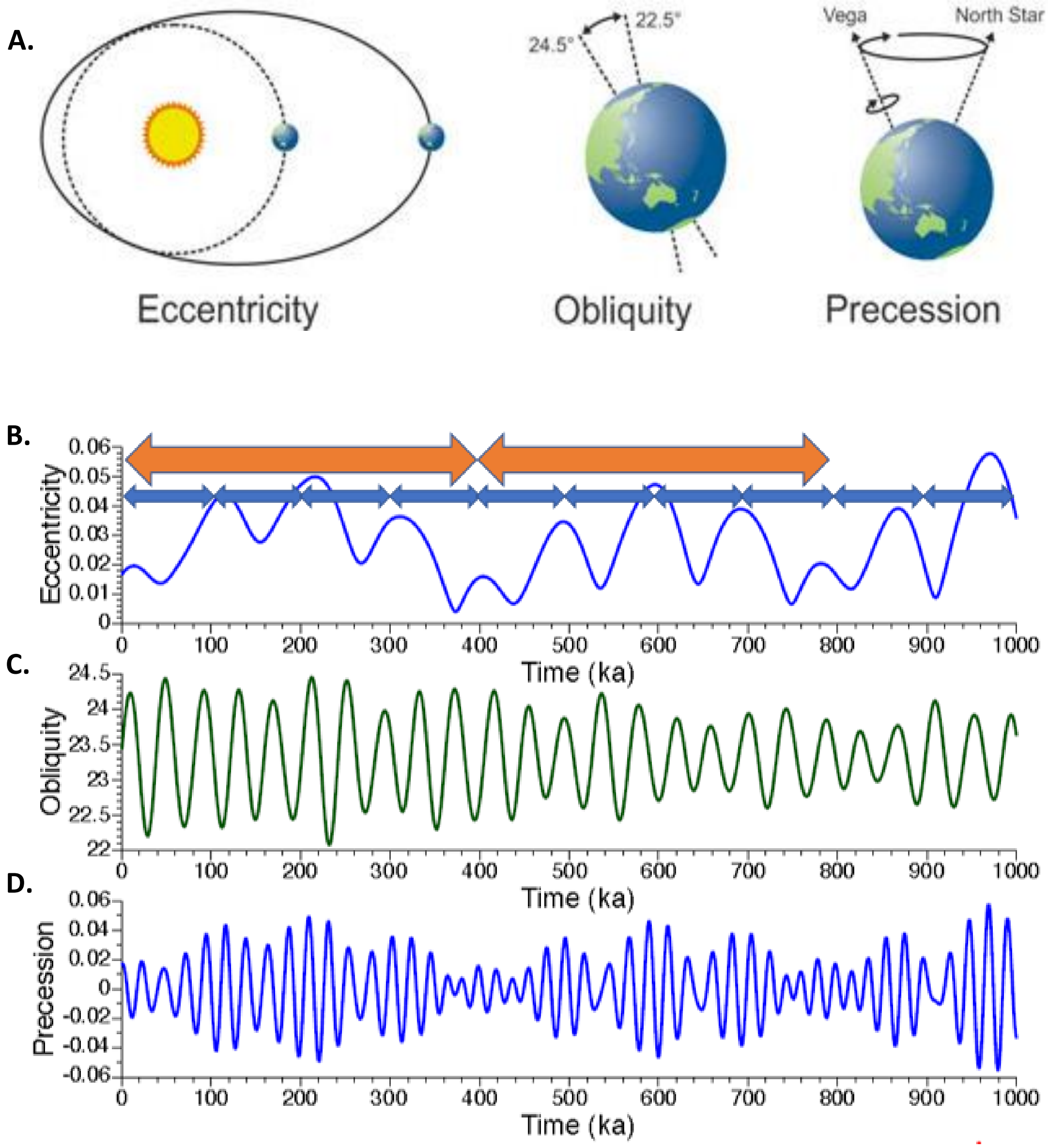

Figure 4: A. Earth's change in orientation with respect to the Sun is caused by three astronomical parameters, orbital eccentricity, obliquity (or axial tilt), and axial precession. B. Orbital eccentricity variation showing 100 kyr short eccentricity cycles (blue arrows) and 400 kyr long eccentricity cycles (orange arrows). C. 41 kyr obliquity cycles. D. 23 kyr and 19 kyr precession cycles. Cycle periods are representative of present-day Milankovitch cycles. From http://www.curaeascensao.com.br/gaiaterra_arquivos/gaiaterra/gaiaterra77.html and Meyers, Isoastro Workshop (2016).

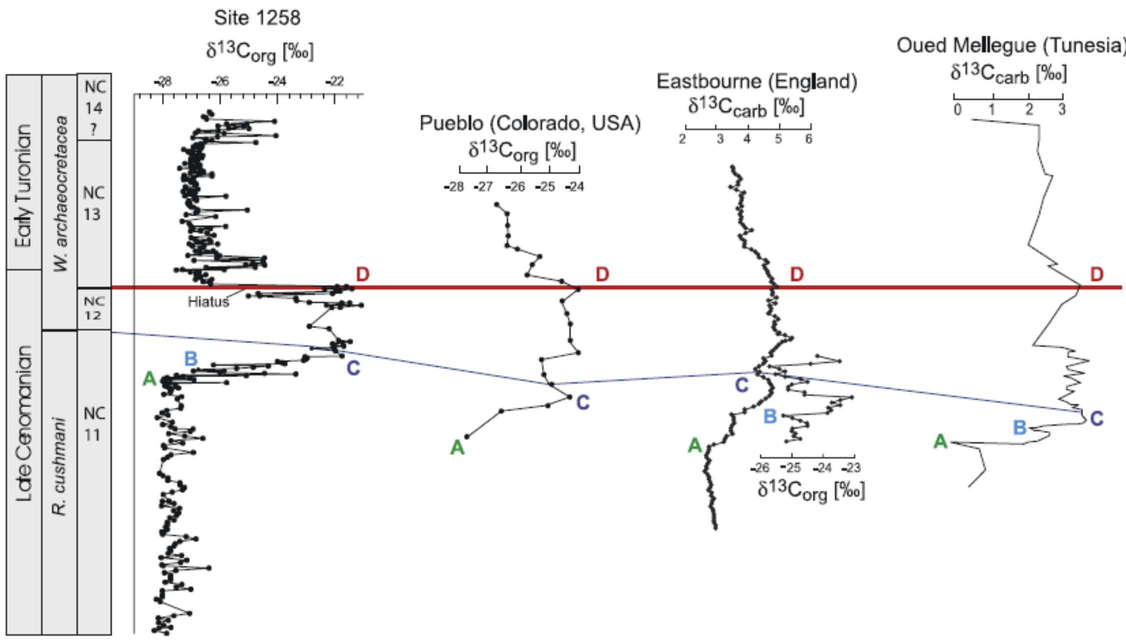

Figure 5: Correlation of carbon isotope data from the Demerara Rise to Pueblo, CO, Eastbourne, UK, and Tunisia. Point D delineates the Cenomanian-Turonian boundary. Points A, B, and C indicate isotopic events identified at both the Demerara Rise and at least one other site. From Erbacher et al. (2005).

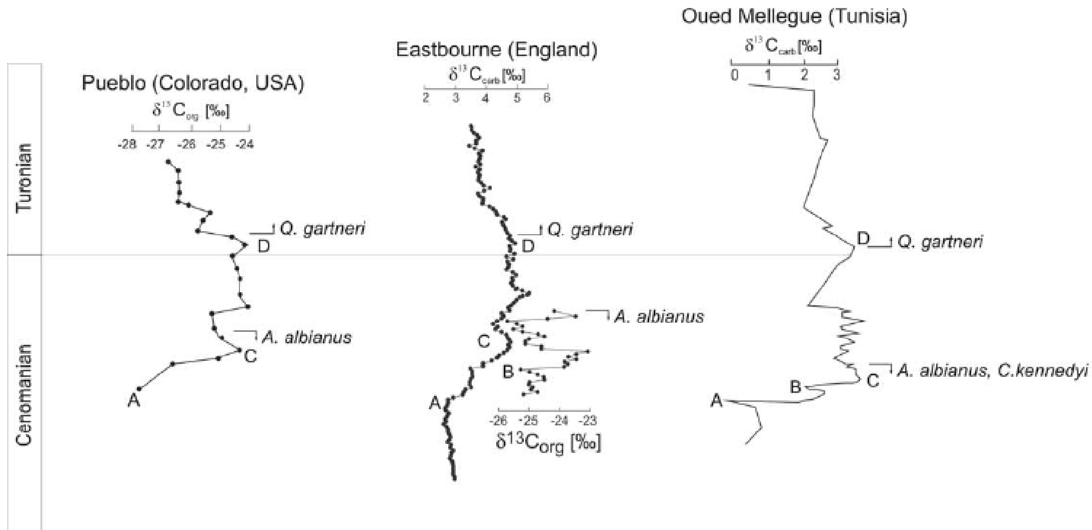

Figure 6: Carbon isotope data adapted from Tsikos et al. (2004) alongside correlation of last occurrence of A. albianus and first occurrence of Q. gartneri. Note difference in placement of C-T boundary, where Tsikos et al. (2005) considers the boundary on point D. From Hardas and Mutterlose (2006).

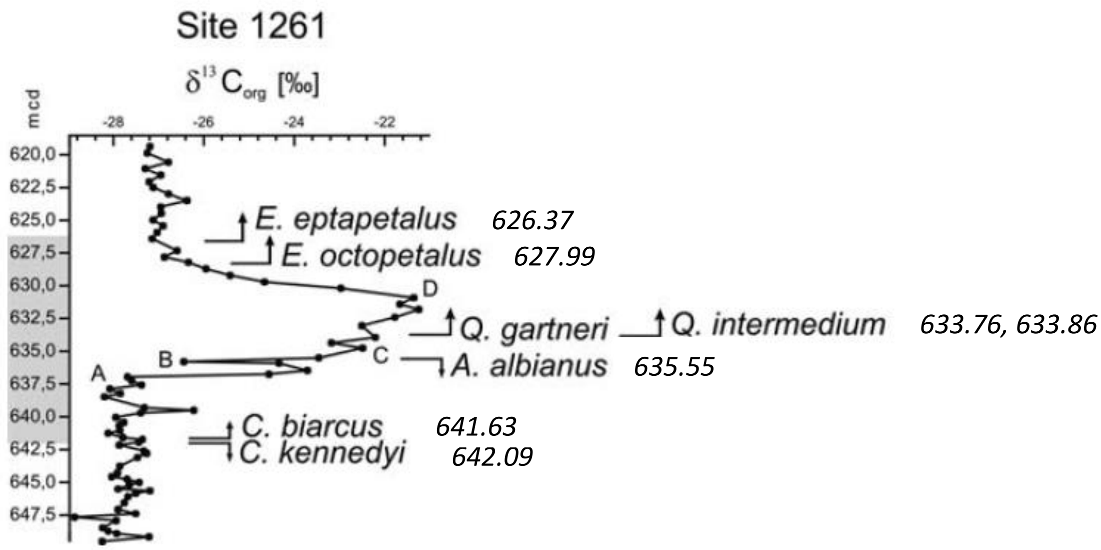

Figure 7: Calcareous nannofossil first and last occurrences at Site 1261 during or near the OAE2 interval, here defined as 637 to 627.99 mcd. Italicized numbers are the exact occurrence depth in mcd. Note FO of *Q. gartneri* near the middle of the CIE, between points C and D. From Hardas and Mutterlose (2006).

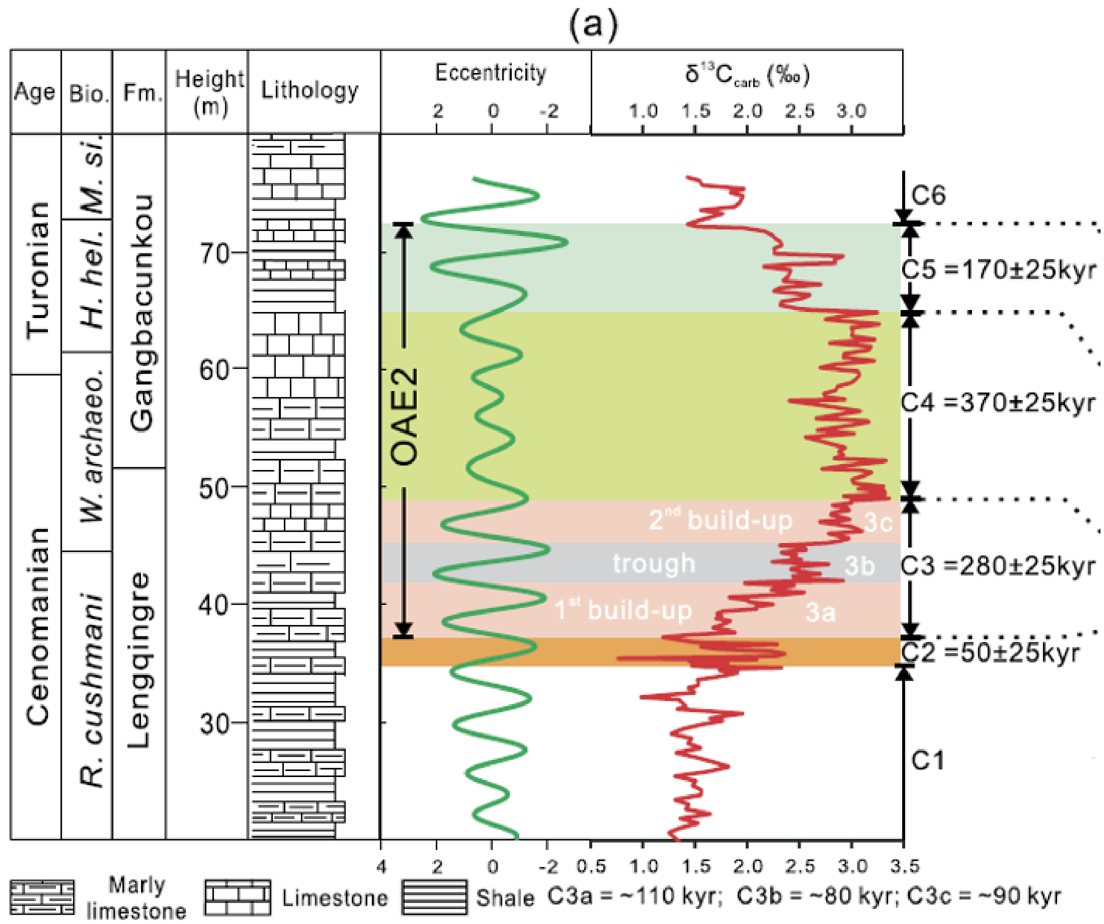

Figure 8: Integrated bio, litho, and chemostratigraphy of the OAE2 interval at Gongzha, Tingri, Tibet. C1 through C6 are carbon isotope stages based on CIE behavior. From Li et al. (2017)

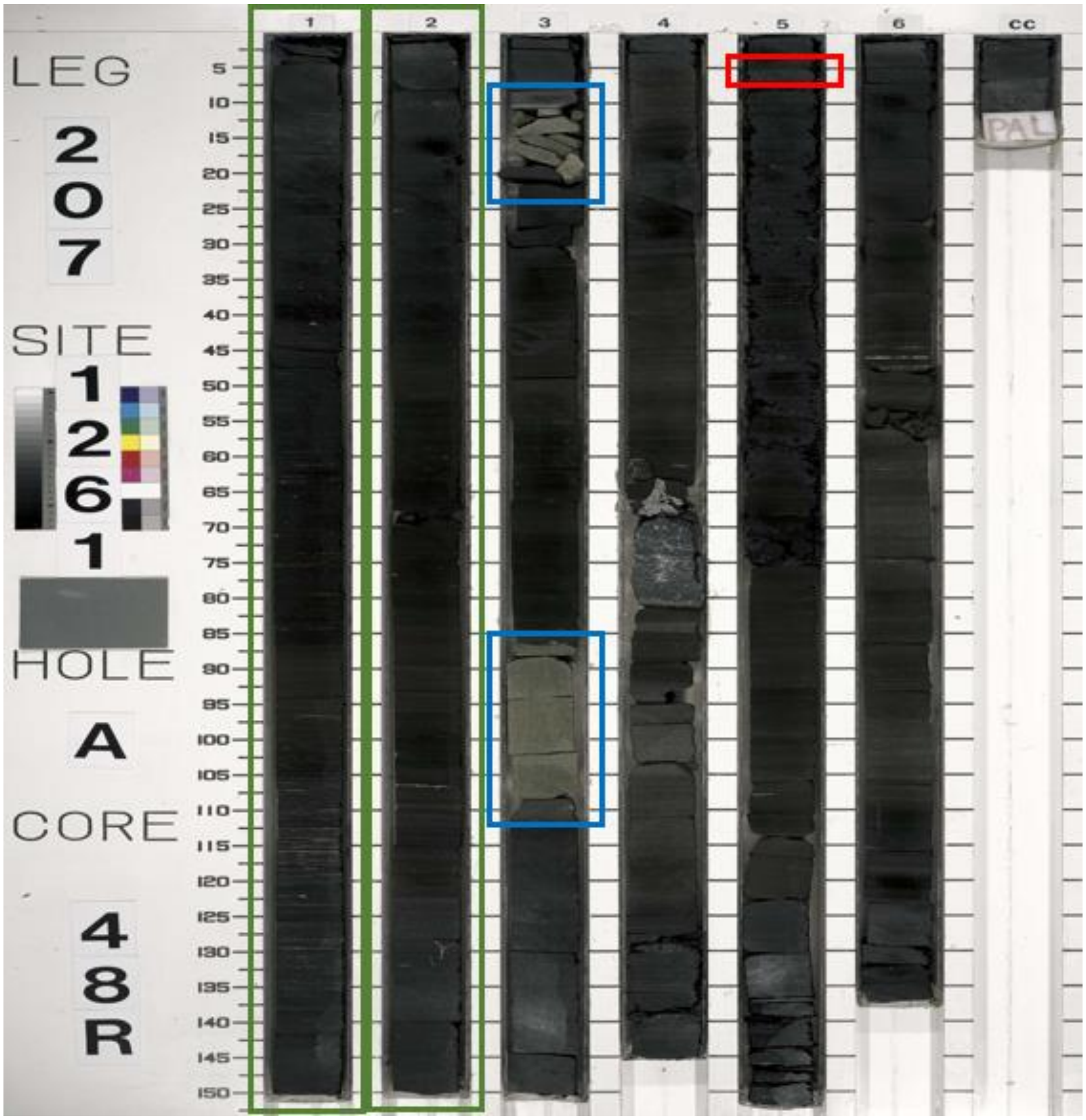

Figure 9: Core box from Site 1261, Core 48A (631.0 to 640.6 mbsf), which contains OAE2 from the top of column 1 to the ~100 cm mark in column 6. Green rectangles show typical organic black shales in the Demerara Rise. Blue rectangles are intervals of sediment with higher carbonate content. Lighter material from 65 to 80 cm in section 4 is diagenetic calcite. The red rectangle is a thin, 1 cm ash layer possibly associated with the Caribbean LIP. Image from http://web.iodp.tamu.edu/janusweb/imaging/photo.cgi?leg=207&site=1261.

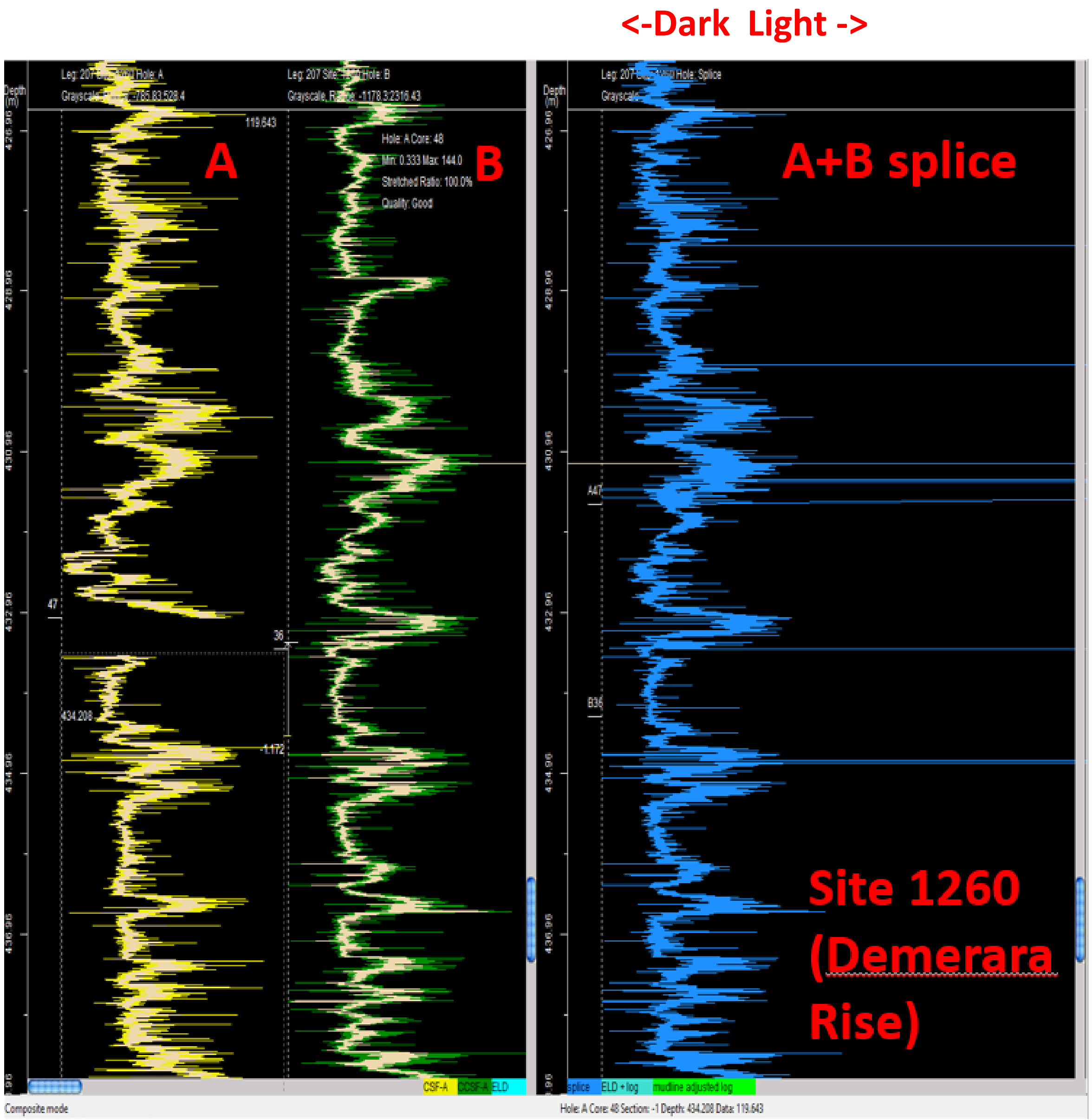

Figure 10: Application of *Correlator* to splice sections of adjacent cores, shown here for Site 1260. The yellow data points are from Core A, the green data points are from Core B, and the blue data points are the composite after splicing the gap at 432 meters depth.

A.

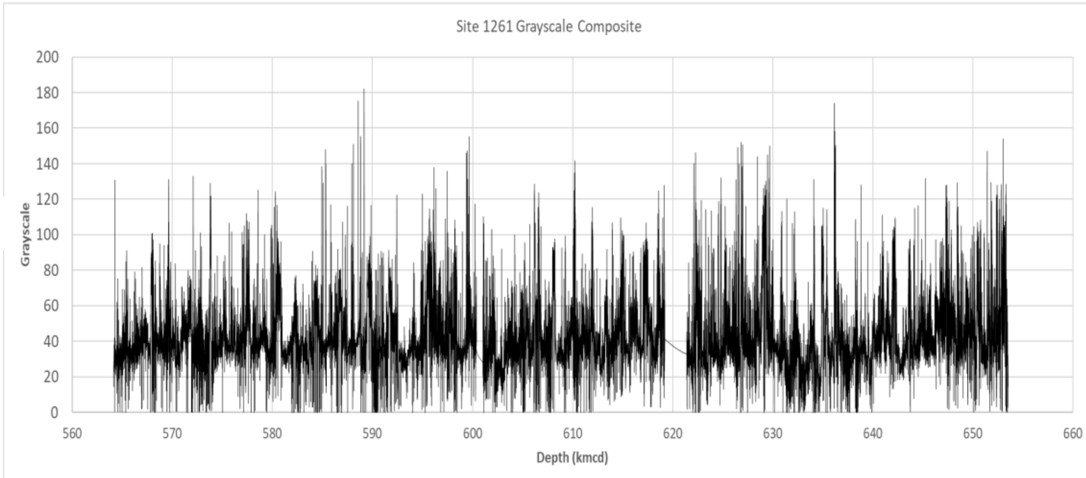

B.

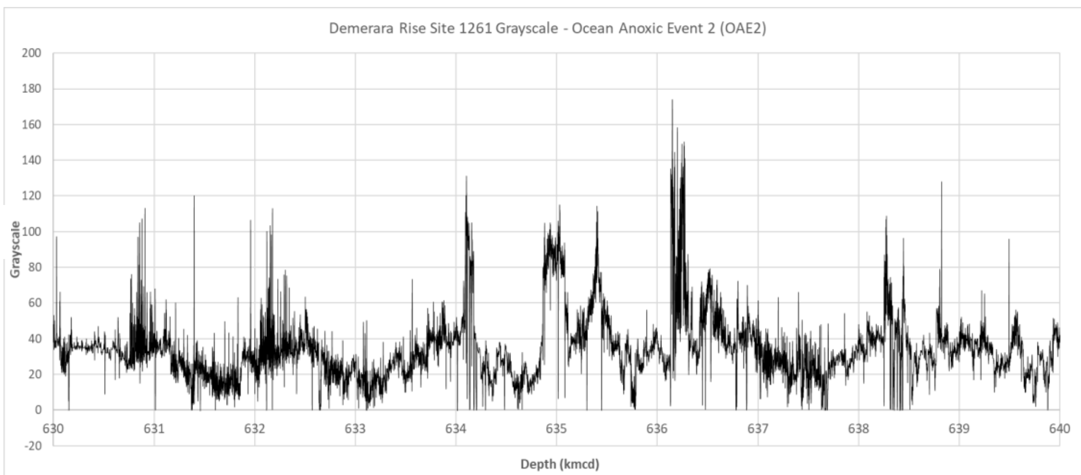

Figure 11: A. Grayscale stratigraphic series using composited and spliced core sections in *Correlator*. Gaps are located between 600.39 and 601.02 kmcd, and 619.2 and 621.4 kmcd. Note meter scale cyclicity throughout interval. Total length of the grayscale scan is 89.38 m. B. Grayscale for OAE2 portion of Site 1261, located between 629.97 and 639.94 kmcd based on carbon isotope values from Erbacher et al. (2005).

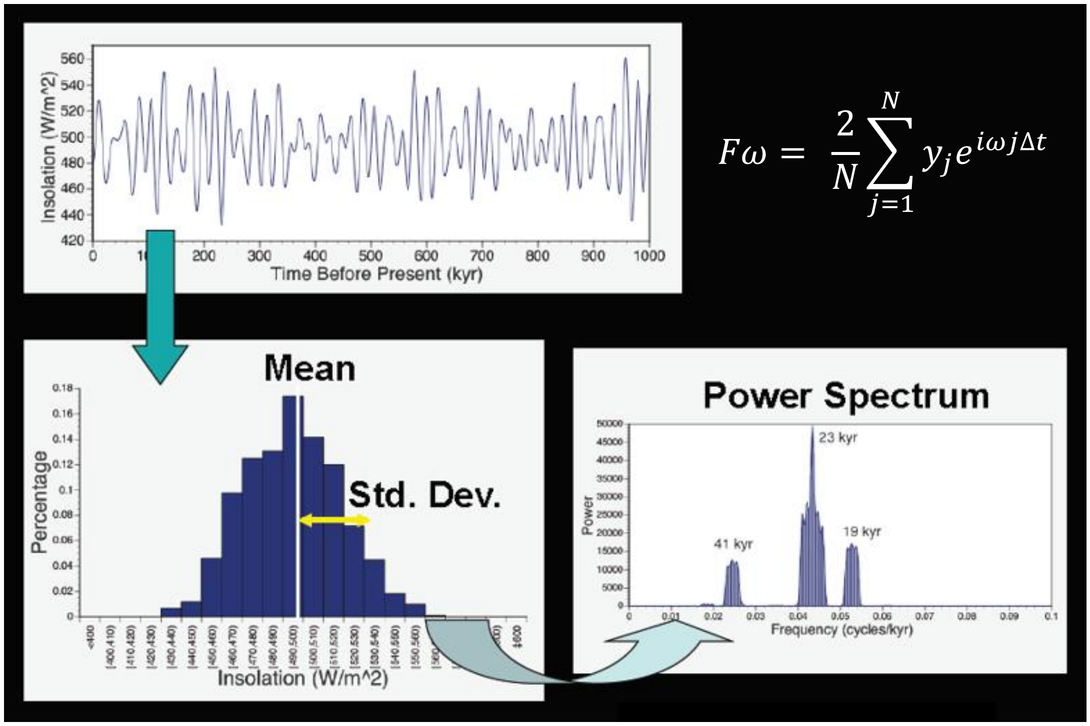

Figure 12: Variance and power spectrum of an insolation time series. Computation of power spectrum is performed via the Fourier transform (top right), which shows the distribution of variance (square of Std. Dev.) as a function of frequency. From Meyers (2016).

A.

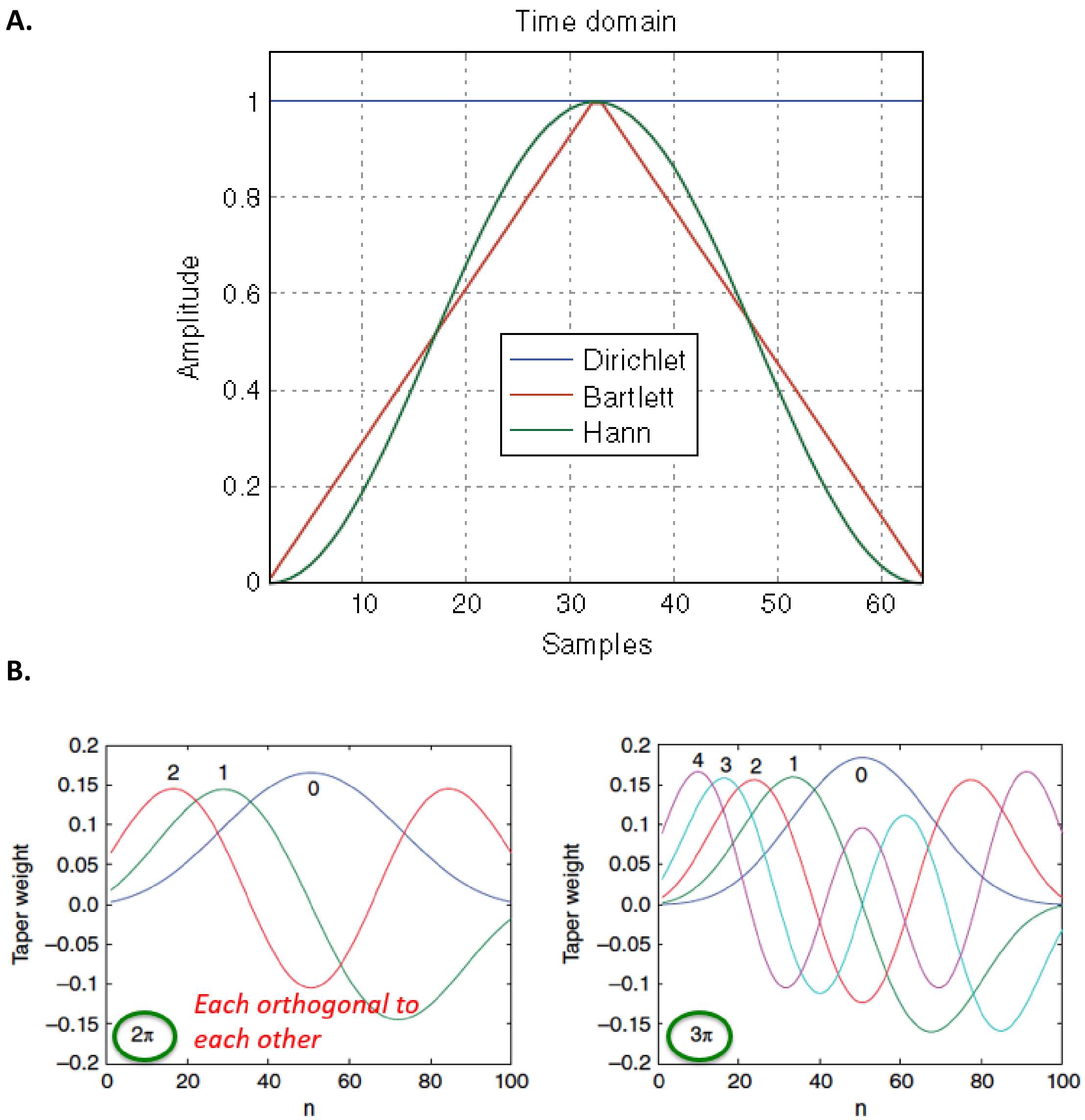

Figure 13: A. Three common data tapers used in spectral analysis. The Dirichlet taper admits the full time series from beginning to end, while the other two tapers significantly down-weight the start and finish of the time series. B. 2π (left) and 3π (right) multiple tapers. Each taper contributes 2 degrees of freedom. From Kodama and Hinnov (2015).

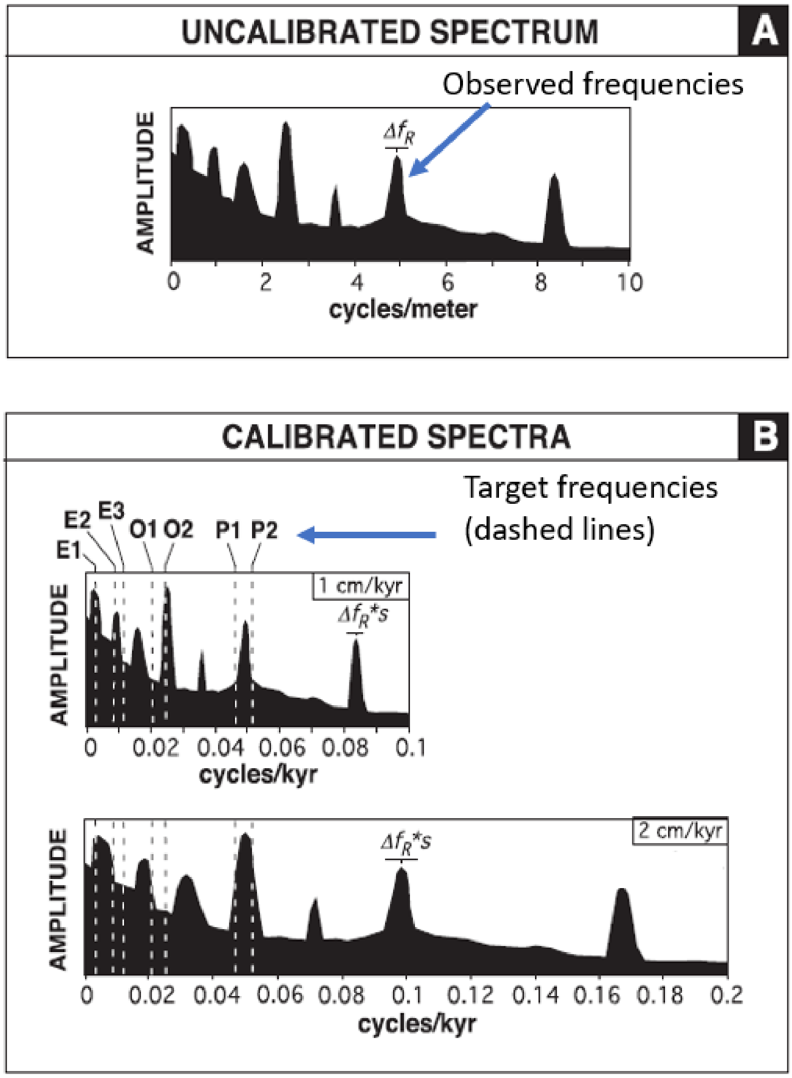

Figure 14: Transformation of observed frequencies (A) in the stratigraphic domain (uncalibrated spectrum to the time domain (B) using two test sedimentation rates 1 cm/kyr and 2 cm/kyr (calibrated spectra. The spectrum which has the lowest spectral misfit between the observed frequencies and the target Milankovitch frequencies E1, E2, E3 (eccentricity), O1, O2 (obliquity), P1, and P2 (precession), is the more likely sedimentation rate for the stratigraphic series. From Meyers and Sageman (2007).

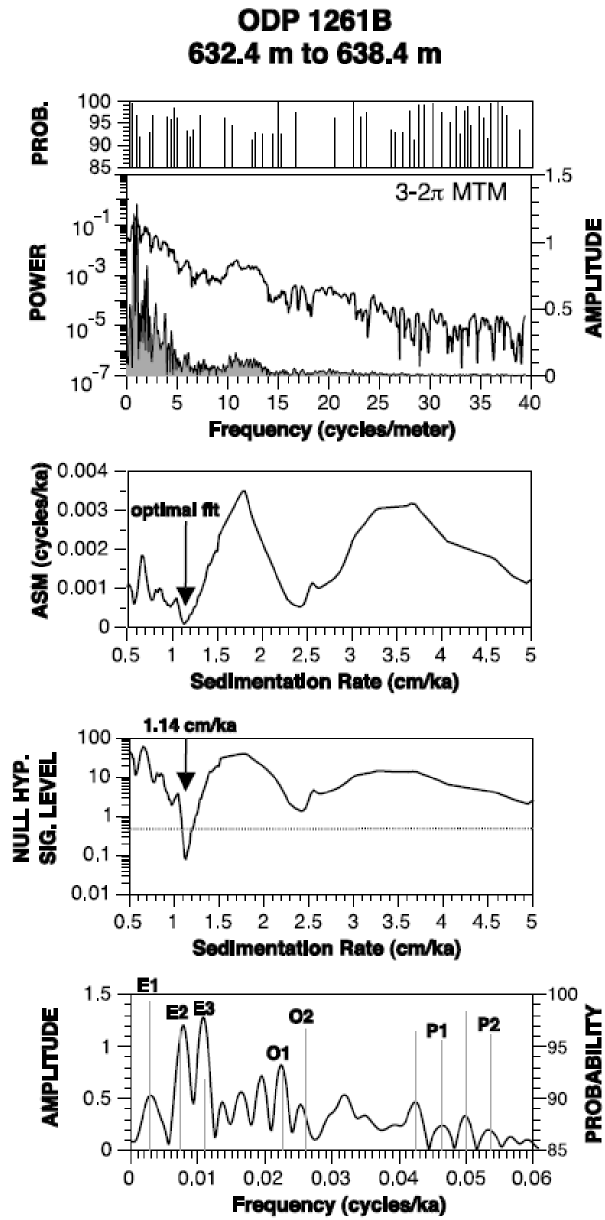

Figure 15: Average Spectral Misfit of Site 1261B Formation MicroScanner data. A. 2π MTM power spectrum covering part of the OAE2 interval from 632.4 mbsf to 638.4 mbsf, showing harmonic F-tests at the top. B. ASM metric for 200 test sedimentation rates, showing an optimal fit at 1.14 cm/kyr. C. Monte Carlo simulations indicate fewer than 0.5% below the 0.5% critical level (horizontal dashed line) at 1.14 cm/kyr, where the null hypothesis of "no astronomical forcing" can be rejected. D. The 1.14 cm/kyr sedimentation rate is used to convert the amplitude spectrum to cycles/kyr. E1=405 kyr; E2=128 kyr; E3=95 kyr; O1=48 kyr; O2=37.6 kyr; P1=23 kyr; P2=18 kyr. From Meyers et al. (2012b).

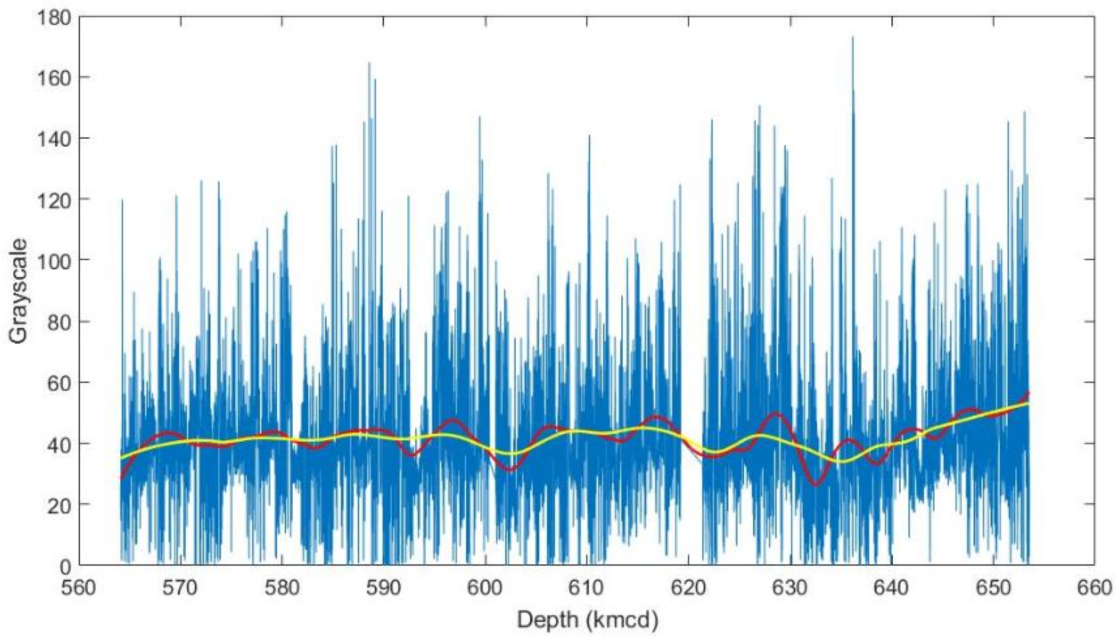

Figure 16: 1261 Grayscale stratigraphic series (blue) showing 10m (red) and 20m (yellow) window LOESS curves.

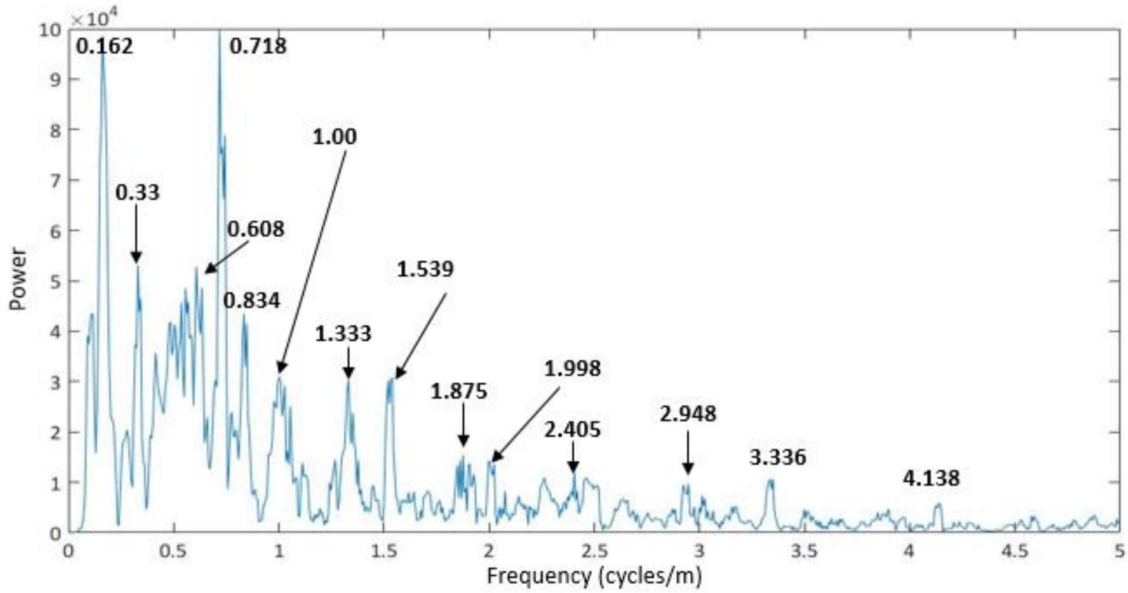

Figure 17: 2π MTM power spectrum of 89.38-m laminated black shale interval showing peaks in cycles/m. Labels are frequency in cycles per meter.

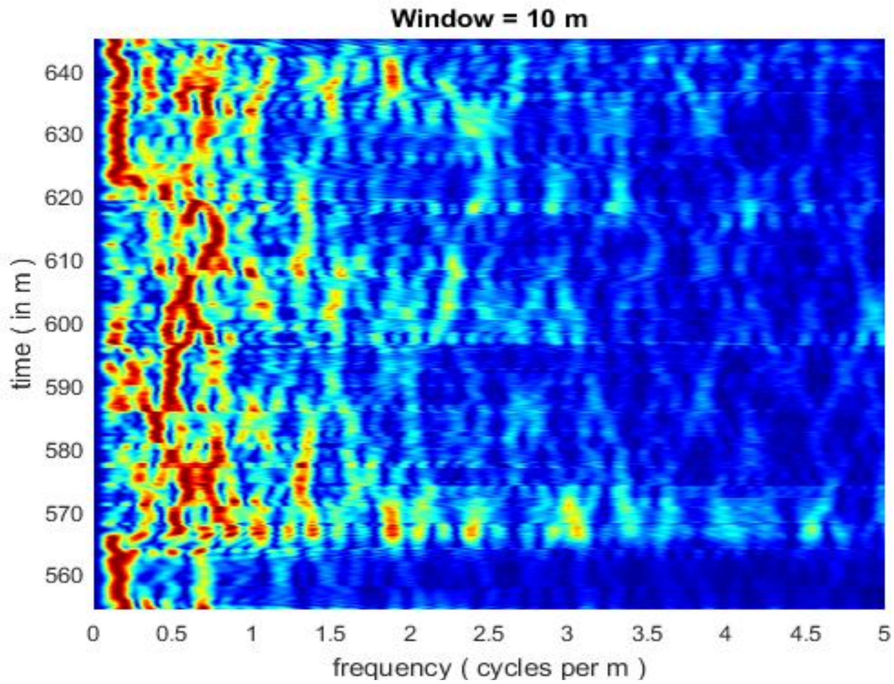

Figure 18: Evolutionary FFT spectrogram for entire 100.15-m grayscale scan of Site 1261, 554.2 to 654.35 kmcd. Blue tones suggest no or low power, while red tones indicate high power. Note switches in dominant frequency between long and short orbital eccentricity frequency bands (0.16 cycles/m and 0.5 to 0.6 cycles/m)

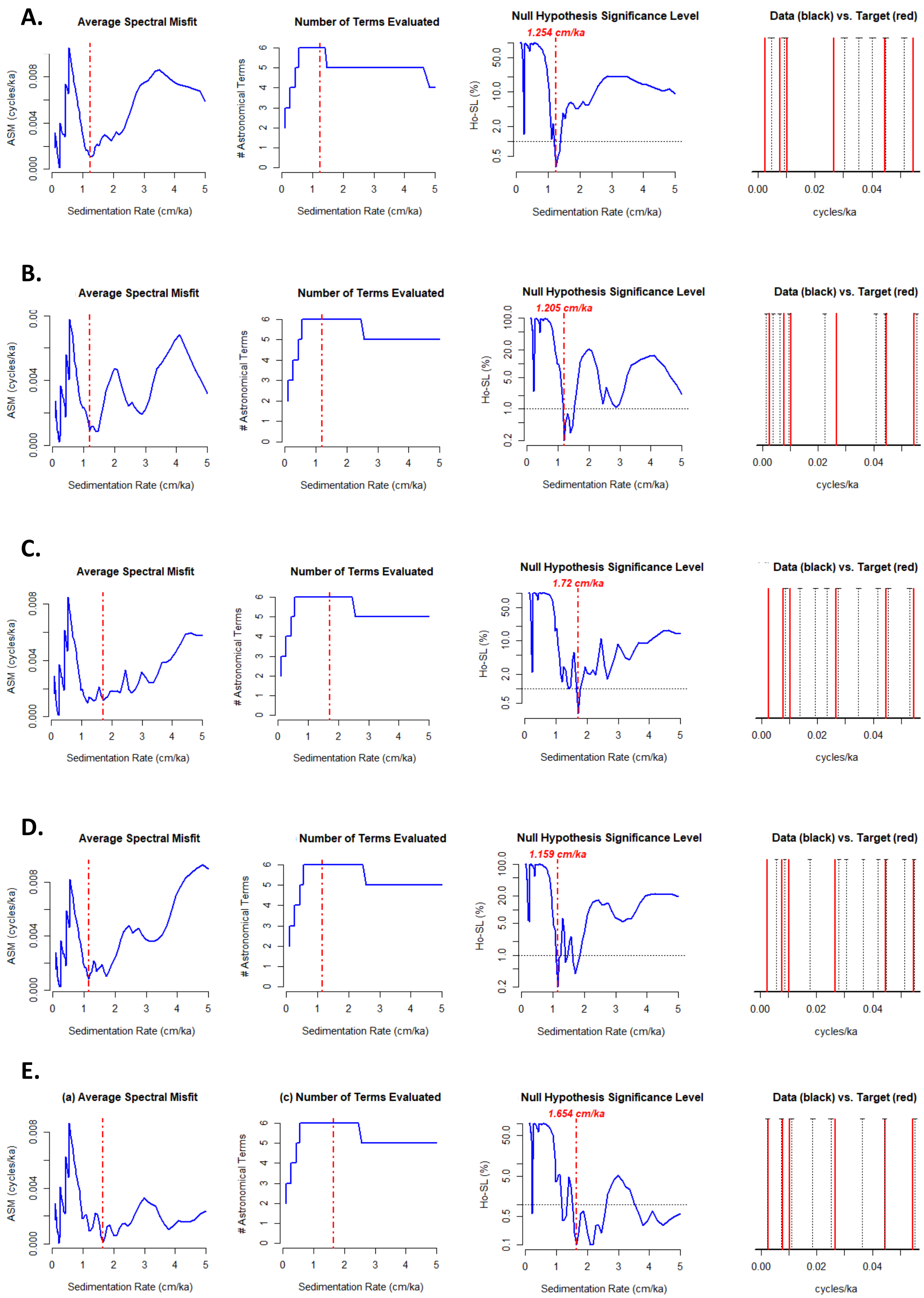
A.
Average Spectral Misfit
ASM (cycles/ka)
Sedimentation Rate (cm/ka)
Number of Terms Evaluated
Astronomical Terms
Sedimentation Rate (cm/ka)
Null Hypothesis Significance Level
1.254 cm/ka
Ho-SL (%)
Sedimentation Rate (cm/ka)
Data (black) vs. Target (red)
cycles/ka
B.
Average Spectral Misfit
ASM (cycles/ka)
Sedimentation Rate (cm/ka)
Number of Terms Evaluated
Astronomical Terms
Sedimentation Rate (cm/ka)
Null Hypothesis Significance Level
1.205 cm/ka
Ho-SL (%)
Sedimentation Rate (cm/ka)
Data (black) vs. Target (red)
cycles/ka
C.
Average Spectral Misfit
ASM (cycles/ka)
Sedimentation Rate (cm/ka)
Number of Terms Evaluated
Astronomical Terms
Sedimentation Rate (cm/ka)
Null Hypothesis Significance Level
1.72 cm/ka
Ho-SL (%)
Sedimentation Rate (cm/ka)
Data (black) vs. Target (red)
cycles/ka
D.
Average Spectral Misfit
ASM (cycles/ka)
Sedimentation Rate (cm/ka)
Number of Terms Evaluated
Astronomical Terms
Sedimentation Rate (cm/ka)
Null Hypothesis Significance Level
1.159 cm/ka
Ho-SL (%)
Sedimentation Rate (cm/ka)
Data (black) vs. Target (red)
cycles/ka
E.
(a) Average Spectral Misfit
ASM (cycles/ka)
Sedimentation Rate (cm/ka)
(c) Number of Terms Evaluated
Astronomical Terms
Sedimentation Rate (cm/ka)
Null Hypothesis Significance Level
1.654 cm/ka
Ho-SL (%)
Sedimentation Rate (cm/ka)
Data (black) vs. Target (red)
cycles/ka

F.

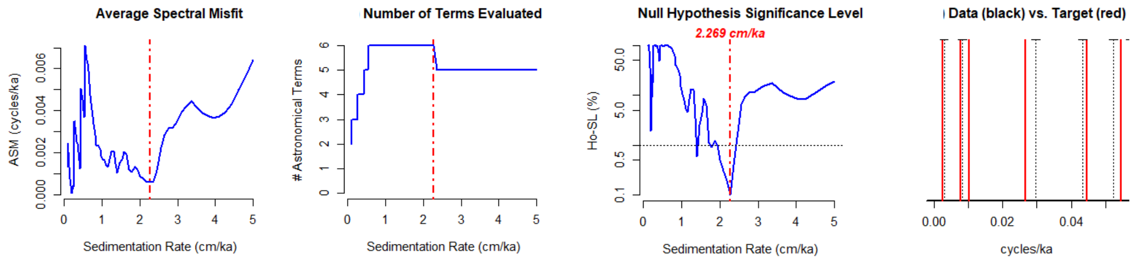
Average Spectral Misfit
ASM (cycles/ka)
Sedimentation Rate (cm/ka)
Number of Terms Evaluated
Astronomical Terms
Sedimentation Rate (cm/ka)
Null Hypothesis Significance Level
2.269 cm/ka
Ho-SL (%)
Sedimentation Rate (cm/ka)
Data (black) vs. Target (red)
cycles/ka

G.

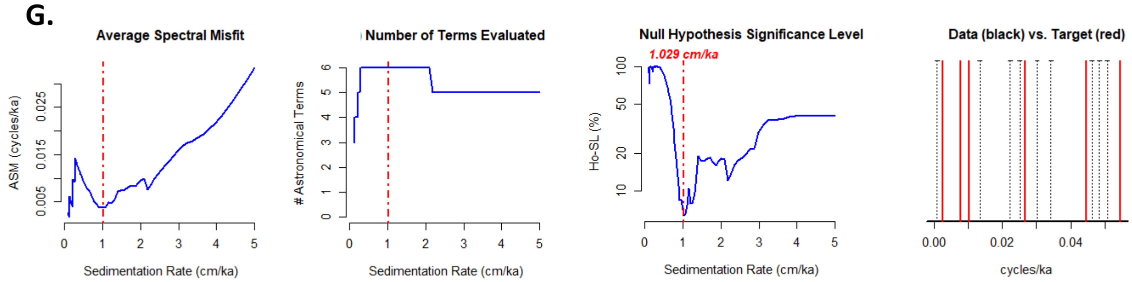
Average Spectral Misfit
ASM (cycles/ka)
Sedimentation Rate (cm/ka)
Number of Terms Evaluated
Astronomical Terms
Sedimentation Rate (cm/ka)
Null Hypothesis Significance Level
1.029 cm/ka
Ho-SL (%)
Sedimentation Rate (cm/ka)
Data (black) vs. Target (red)
cycles/ka

H.

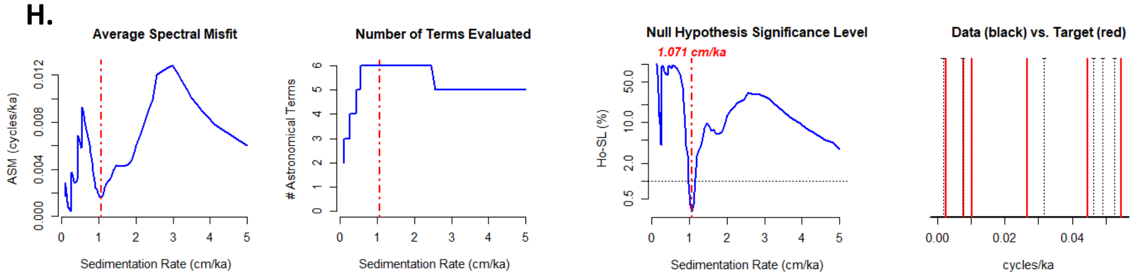
Average Spectral Misfit
ASM (cycles/ka)
Sedimentation Rate (cm/ka)
Number of Terms Evaluated
Astronomical Terms
Sedimentation Rate (cm/ka)
Null Hypothesis Significance Level
1.071 cm/ka
Ho-SL (%)
Sedimentation Rate (cm/ka)
Data (black) vs. Target (red)
cycles/ka

I.

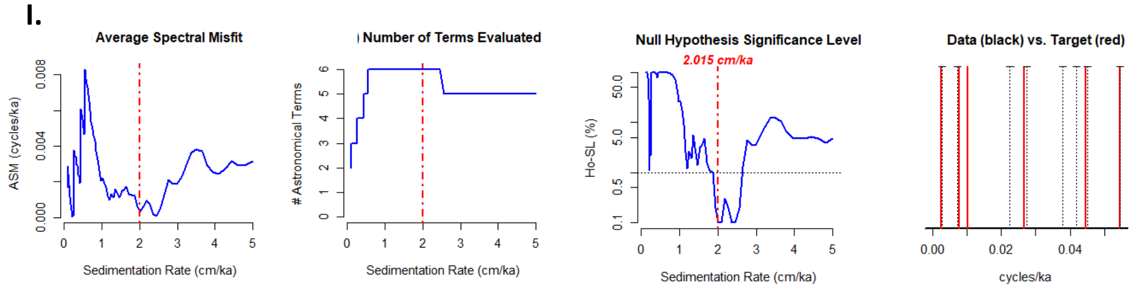
Average Spectral Misfit
ASM (cycles/ka)
Sedimentation Rate (cm/ka)
Number of Terms Evaluated
Astronomical Terms
Sedimentation Rate (cm/ka)
Null Hypothesis Significance Level
2.015 cm/ka
Ho-SL (%)
Sedimentation Rate (cm/ka)
Data (black) vs. Target (red)
cycles/ka

J.

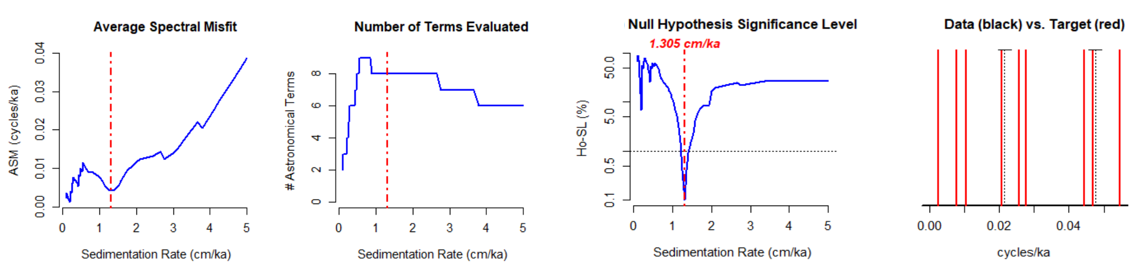
Average Spectral Misfit
ASM (cycles/ka)
Sedimentation Rate (cm/ka)
Number of Terms Evaluated
Astronomical Terms
Sedimentation Rate (cm/ka)
Null Hypothesis Significance Level
1.305 cm/ka
Ho-SL (%)
Sedimentation Rate (cm/ka)
Data (black) vs. Target (red)
cycles/ka

K.

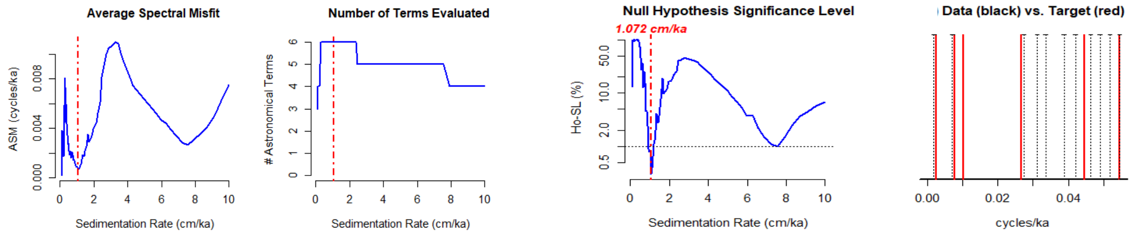

Figure 19: Average spectral misfit tests for 10-meter segments of the 1261 grayscale series. Graphs from left to right: ASM metric, number of terms evaluated, null hypothesis significance interval, and observed (red lines) vs. target (dashed lines) frequencies. A. 564.13 to 570 kmcd; B. 570 to 580 kmcd; C. 580 to 590 kmcd; D. 590 to 600 kmcd; E. 600 to 610 kmcd; F. 610 to 620 kmcd; G. 620 to 630 kmcd; H. 630 to 640 kmcd; I. 640 to 650 kmcd; J. 650 to 653.51 kmcd; and K. Post-OAE2 section of 554.2 to 564.12 kmcd. The optimal sedimentation rates (indicated in the null hypothesis plots) are assembled in Table 2.

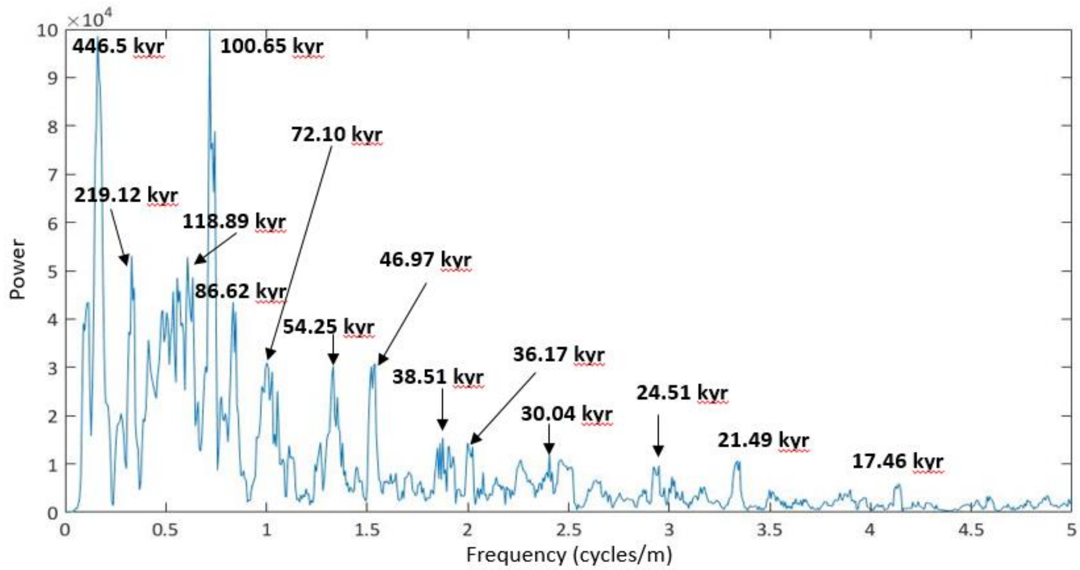

Figure 20: 2π MTM power spectrum of the 89.38-m laminated black shale interval based on 1.384 cm/ka average sedimentation rate. Proposed Milankovitch peaks are: 446.5 kyr long eccentricity, 100.65 kyr short eccentricity, 46.97 kyr obliquity, and 21.49 kyr precession (see Table 2).

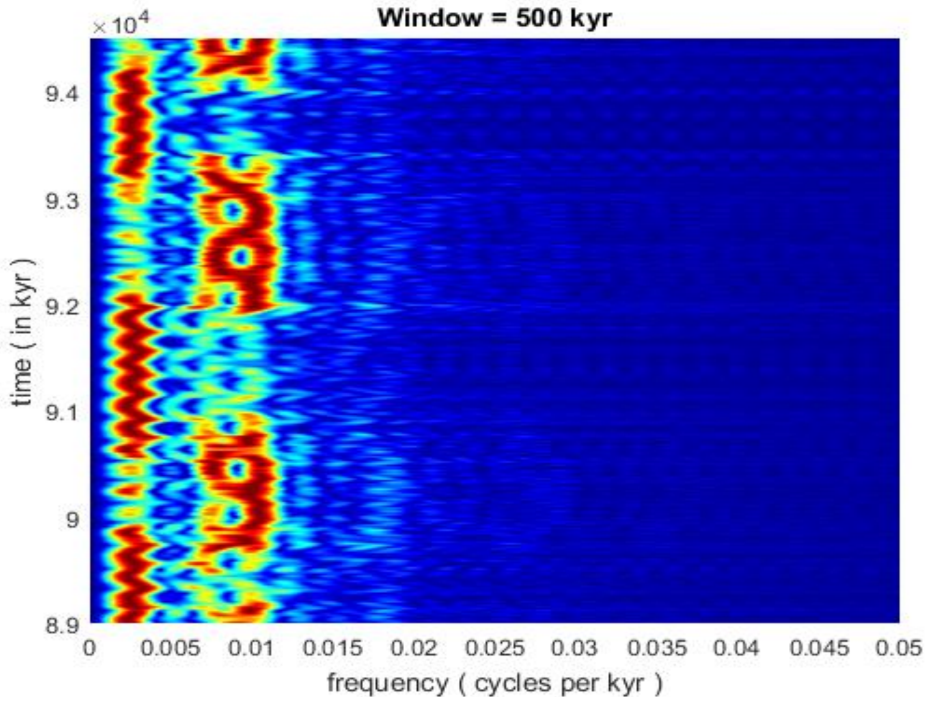

Figure 21: Evolutionary FFT spectrogram for idealized theoretical eccentricity published by Laskar (2004). Similarities of long and short eccentricity behavior and braided pattern of short eccentricity can be observed.

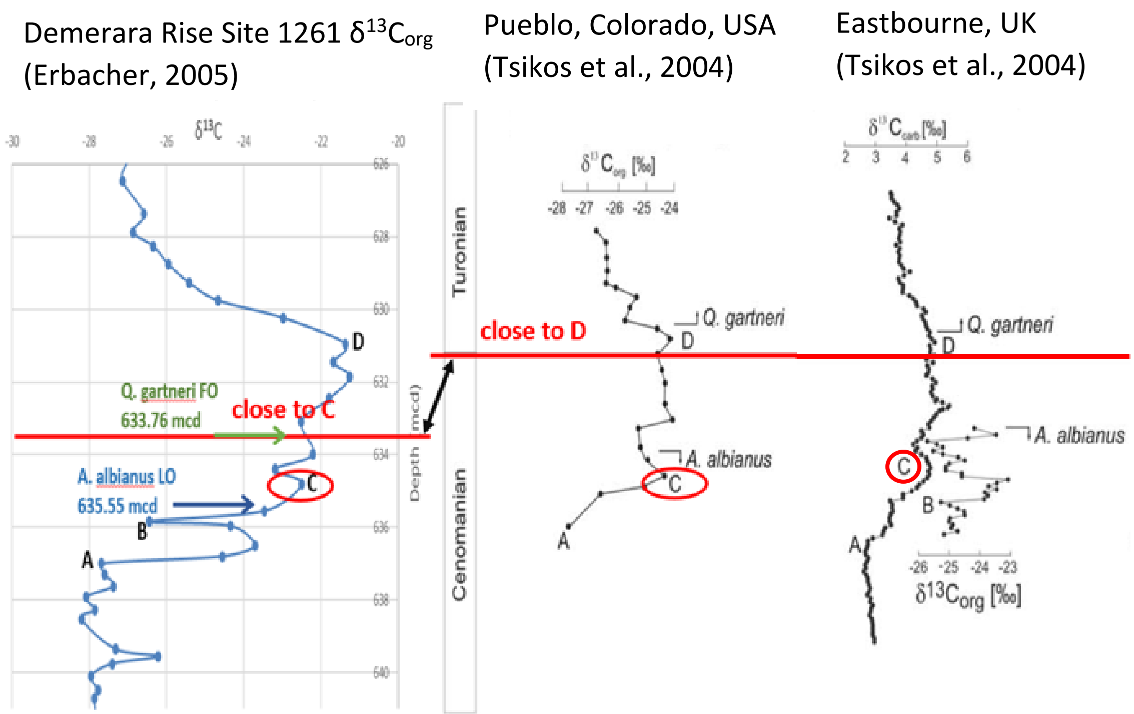

Figure 22: Carbon isotope values from Site 1261 (Erbacher et al., 2005), the outcrop section at Pueblo, Colorado in the Western Interior Seaway, and Eastbourne UK (Tsikos et al., 2004). The Pueblo, Colorado location is the international GSSP for the Cenomanian-Turonian boundary. Calcareous nannofossils *Q. gartneri* and *A. albianus* are plotted alongside, showing disagreements in occurrence depth with respect to the carbon isotope excursion and the C-T boundary.

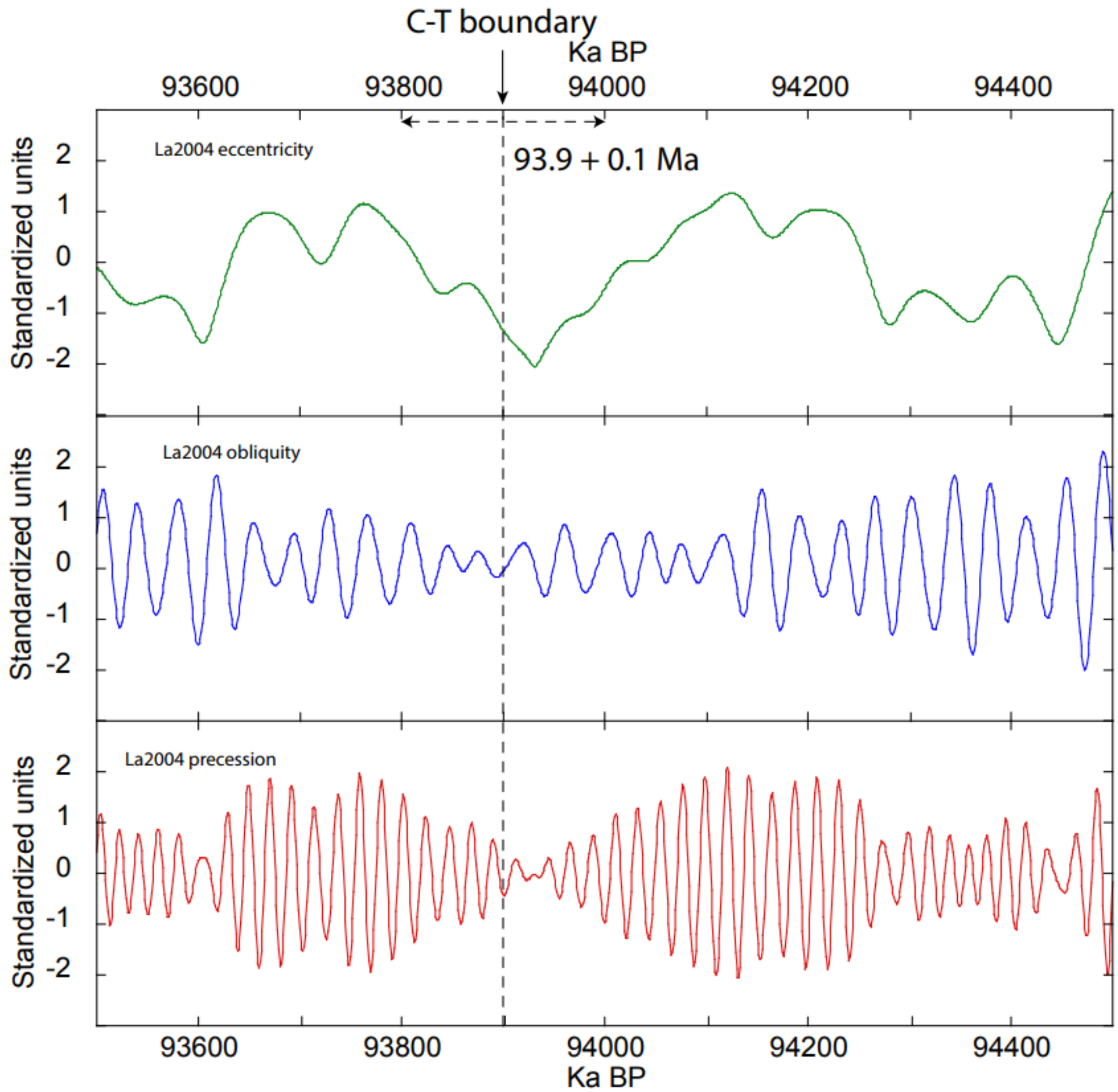

Figure 23: Orbital eccentricity, obliquity, and precession index surrounding the C-T boundary. Note the end of a long eccentricity cycle at ~93.9 Ma that coincides with current C-T boundary (green), and weakening of obliquity (blue) and precession index (red) signals amplitudes also at this time. From the astronomical solution of Laskar et al. (2004).

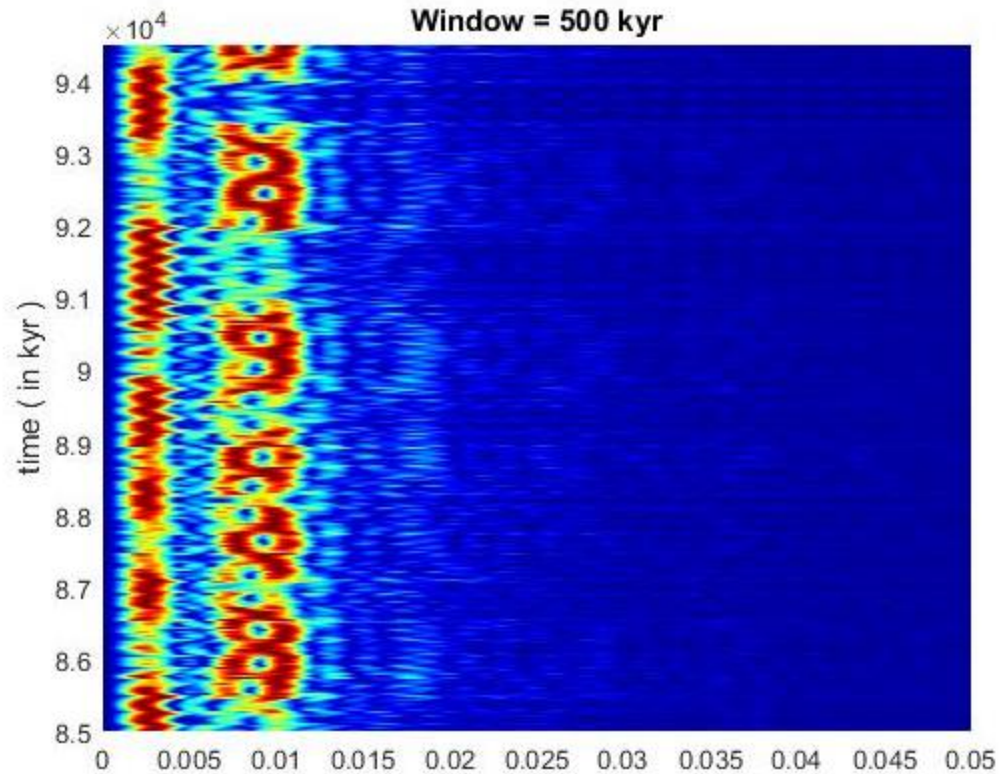

Figure 24: Theoretical La2004 orbital eccentricity spectrogram with a running 500 kyr window depicting eccentricity power over a 10 myr span from 95 to 85 Ma. Five to six long eccentricity-dominated intervals are visible here, while there are only three of these sections in the black shale spectrogram from Site 1261 (compare with Figure 18).

APPENDIX A

Generating grayscale data using *ImageJ*

Open a jpg file with the core image in Imagej:

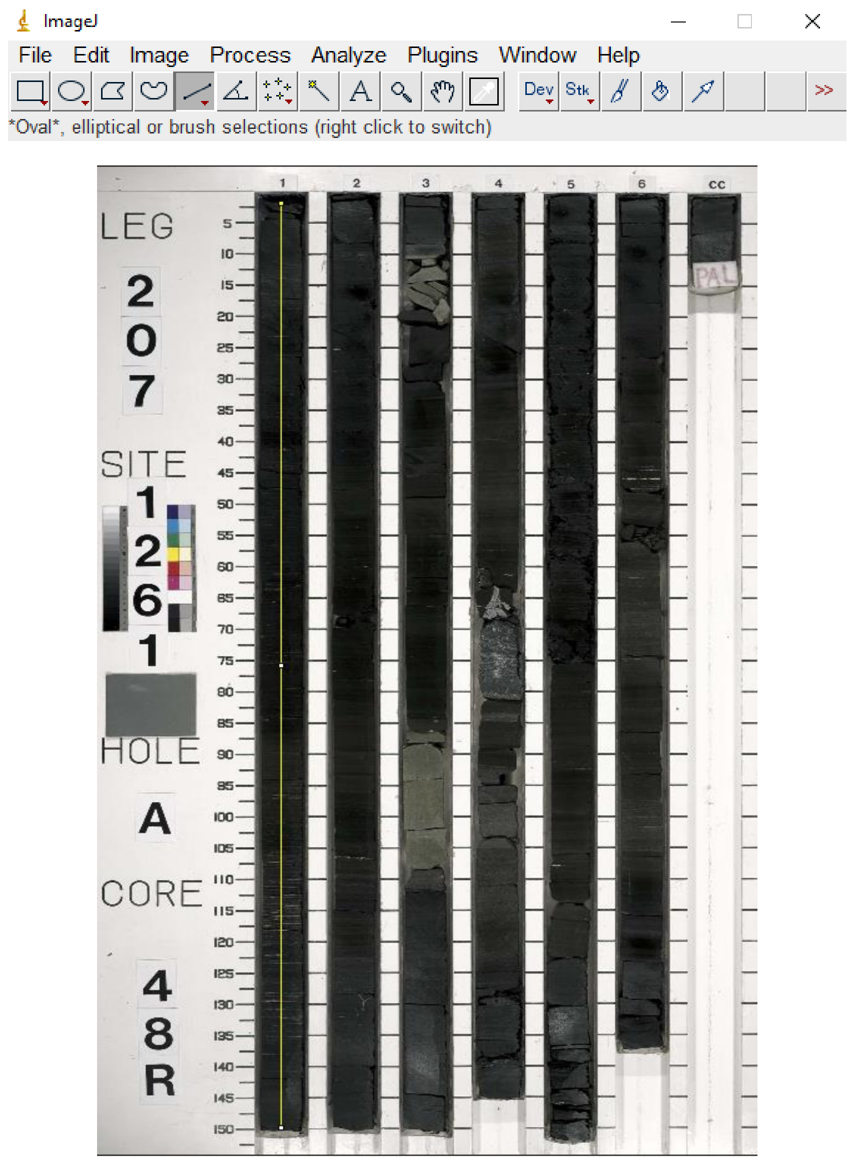

Note yellow line crosses through the middle of the section. For section 1, the line does not start at the very top of the section as the first couple centimeters do not have core. This is factored into the sampling rate. Image from http://web.iodp.tamu.edu/janusweb/imaging/photo.cgi?leg=207&site=1261

From toolbar: Analyze -> Plot Profile

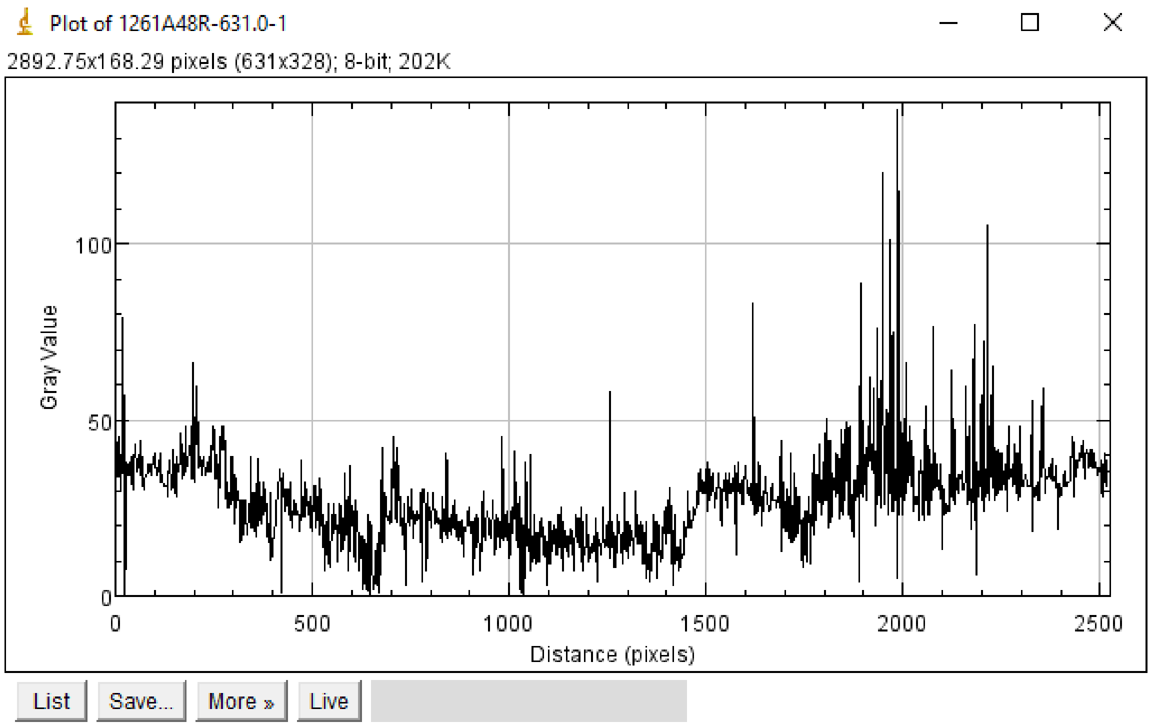

Save the data to a text file, or copy paste into Excel. These grayscale values range from 0 (black) to 255 (white), with respect to "pixel number" along the scan, which must be converted to core depth.

APPENDIX B

Notes on Compositing and Splicing Data with *Correlator*

For video guides on how to use *Correlator*, go to
http://www.corewall.org/documents/index.html

Importing Data:

To load in data to Correlator, a CSV file must include headings in a particular manner:

	A	B	C	D	E	F	G	H	I	J	K
1	Exp	Site	Hole	Core	CoreType	Section	TopOffset	BottomOf	Depth	Data	
2	207	1260	B	30	D	1	0	0	386.5	120	
3	207	1260	B	30	D	1	0.000587	0.000587	386.5006	104	
4	207	1260	B	30	D	1	0.001173	0.001173	386.5012	98	
5	207	1260	B	30	D	1	0.00176	0.00176	386.5018	122	
6	207	1260	B	30	D	1	0.002347	0.002347	386.5023	115	
7	207	1260	B	30	D	1	0.002933	0.002933	386.5029	108.333	
8	207	1260	B	30	D	1	0.00352	0.00352	386.5035	159	
9	207	1260	B	30	D	1	0.004106	0.004106	386.5041	175	
10	207	1260	B	30	D	1	0.004693	0.004693	386.5047	168	
11	207	1260	B	30	D	1	0.00528	0.00528	386.5053	135	
12	207	1260	B	30	D	1	0.005866	0.005866	386.5059	113	
13	207	1260	B	30	D	1	0.006453	0.006453	386.5065	117	
14	207	1260	B	30	D	1	0.00704	0.00704	386.507	123	
15	207	1260	B	30	D	1	0.007626	0.007626	386.5076	119	
16	207	1260	B	30	D	1	0.008213	0.008213	386.5082	125	
17	207	1260	B	30	D	1	0.008799	0.008799	386.5088	109	
18	207	1260	B	30	D	1	0.009386	0.009386	386.5094	102	
19	207	1260	B	30	D	1	0.009973	0.009973	386.51	118	
20	207	1260	B	30	D	1	0.010559	0.010559	386.5106	135	
21	207	1260	B	30	D	1	0.011146	0.011146	386.5111	131	
22	207	1260	B	30	D	1	0.011733	0.011733	386.5117	120	
23	207	1260	B	30	D	1	0.012319	0.012319	386.5123	117	
24	207	1260	B	30	D	1	0.012906	0.012906	386.5129	124	
25	207	1260	B	30	D	1	0.013492	0.013492	386.5135	124	

- CoreType can be given any random letter
- Top and Bottom Offsets are the same formula: depth at data point – uppermost depth. So here, G2 and H2 = I2 – 386.5
- **Depth must be the Y-axis in Correlator**
- Data: Here grayscale, any data must be loaded in under the header “Data”.

Start *Correlator*. The first screen shown is the “Data List” tab on the Data Manager window. Right click on root in the data list tab -> add new data.

Select your CSV file, and the first 30 rows should come up under the “generic data” tab.

Left click on the Data Type column, and select one from the list or click user define to manually label the type of data you are adding.

Make sure the path to the file you are importing is correct at the bottom of the window, and click on Import.

- If you have a lot of data – tens of thousands of rows in Excel – Correlator will take a while to import the data; up to 15 minutes. **High resolution data makes *Correlator* run fairly slowly in every step of the process.**
- You may need to close *Correlator* after loading the first set of data in order to load another set of data from the same site – *Correlator* sometimes thinks you are trying to load the same data twice.

After the data is imported, the Data Manager screen will appear and list your data by Leg (Expedition) and Site.

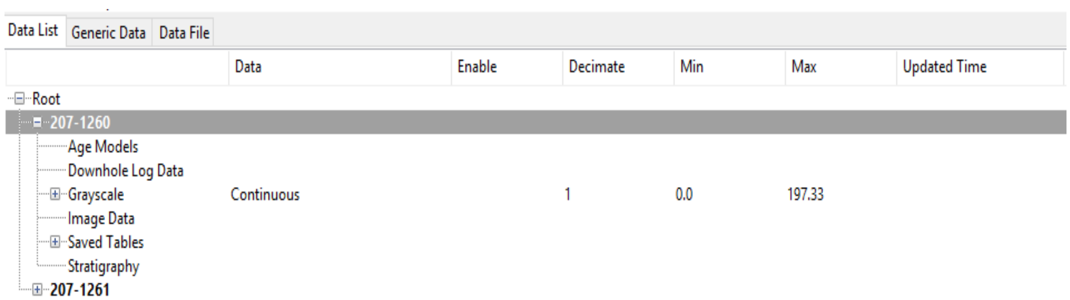

<u>Loading and cleaning up your data:</u>

In the Data List tab, right click on the Leg-Site and choose load. **This can also take a long time with high resolution data, up to 20 minutes.**

Once your data is loaded, you will be brought to the “display” screen. This contains your data versus depth.

Scroll down to your data using the scroll bar in the middle. If there are gaps represented by 0’s or large numbers in your data, you will probably want to cull them.

- Go to the right-hand side of the window, select the "Filter" tab, and use the Cull section to cull or trim your data. Click apply.

- Also in this tab, the data can be tidied up using Gaussian smoothing. Under the "Smooth" section, choose Gaussian type, and a width of 9 to 11 points, Smoothed & Unsmoothed, and click apply.

- **Note: You will have to re-do the cull every time you open *Correlator*.**

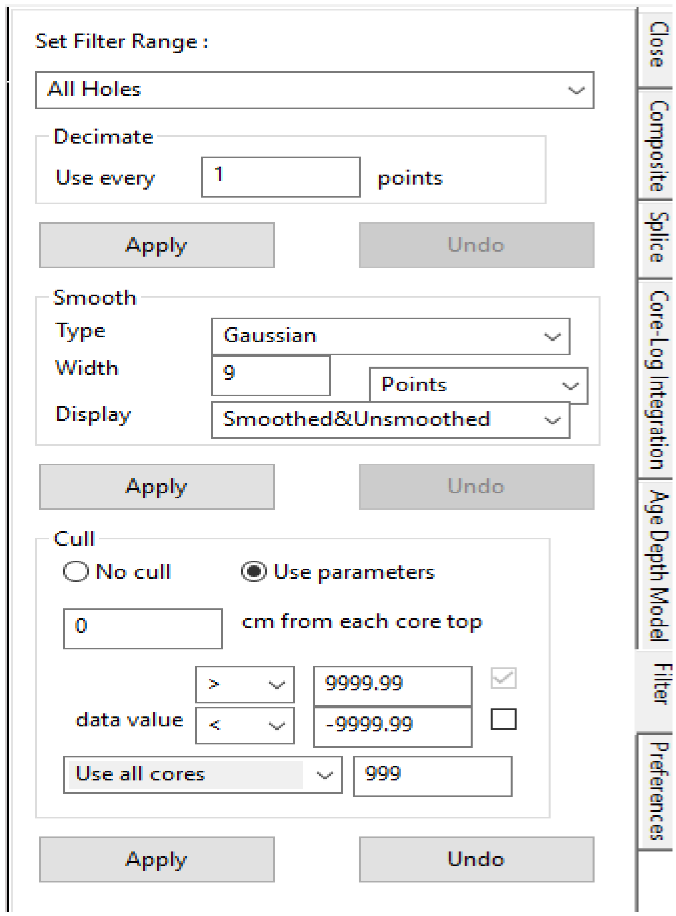

Next, select the preferences tab. If you can't view the smaller changes/cycles in your data, this can be adjusted here.

While in this window, you can deselect the "Splice/Log window". This is not needed yet.

- To expand your data horizontally, change the Variable maximum. Typically, 75 to 150 is fine.

- To zoom in on the data, decrease the max in the Ruler Depth Scale. Any changes to the ruler depth scale will bring the window back to 0m depth, so you will need to scroll back down.

- To zoom out, increase the ruler depth scale.

- **Note: You also will have to re-adjust the Display Range every time you open *Correlator*.**

- The Keyboard Tie Shift Depth Scale options allows you to scroll through your data using the arrow keys – here pressing once on the down arrow will shift the window 0.01m downward.

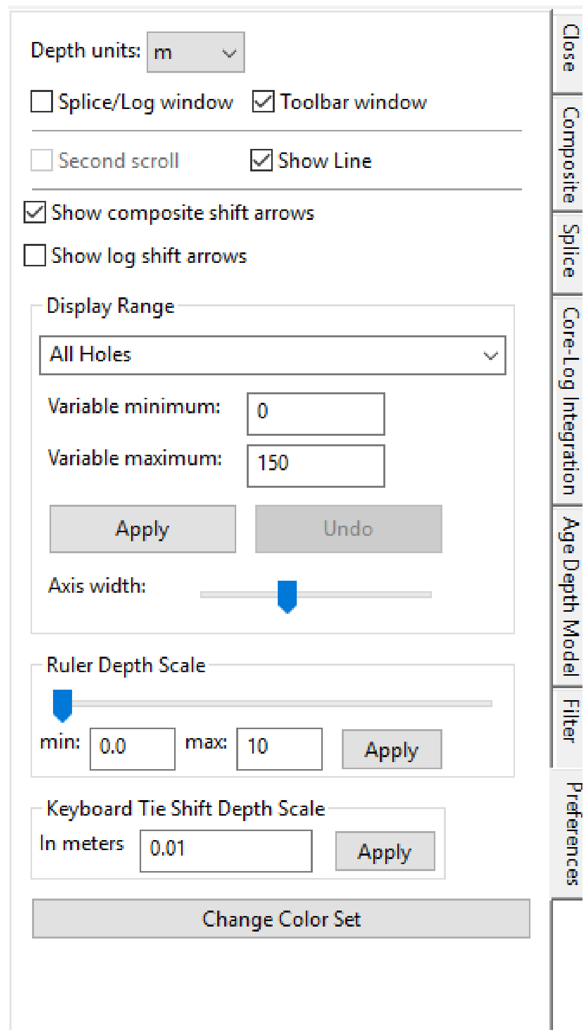

Compositing/Correlating Data:

To create points for correlation between two sets of data, Shift+Left Click on the first set of data, and Shift+Left Click on the second set to create a “tie point” between the two.

- If you have a lot of data, the shift+left click may not take place. Sometimes you have to click several times for the point to show.

- Make sure when clicking, you're clicking on data and not any blank space. *Correlator* will not create a tie point if you click on a space without data. Also, make sure to keep the mouse still when clicking – Correlator will often not create a tie point if the mouse is still moving while clicking**.**
- After the point is created, an overlapping red and white line will display the data from set B overtop of set A.
- **If the tie point isn't exactly where you like it, you can click and drag up and down to adjust.**

If you have lower resolution data, you can use the Composite tab on the right-hand side for an evaluation graph that calculates the best match for your composite based on nearby data points. **However, the graph does not function well with high resolution/millimeter scale data.**

Once the tie point is in the correct position, right click on the green circle of the tie point you just created. It is advised to choose "adjust depth with this core and all below", or you will have core sections that begin to overlap below.

- Alternatively, if you are going back to re-correlate sections farther up or only want to shift one core section, "adjust depth with this core only" is probably the better option.

If at some point you want to move a core section by itself, go to the Composite tab.

At the bottom of this tab, there is the option to "Set by Growth Rate or %"

Here you can shift a selected core by a certain percentage or fixed distance – fixed distance seems to be the more reliable option.

A positive fixed distance shift moves the core down, where a negative shift moves it up.

Correlator may also suggest a shift amount if it sees a nearby location with a strong positive correlation. This also does not seem to work well with high resolution data.

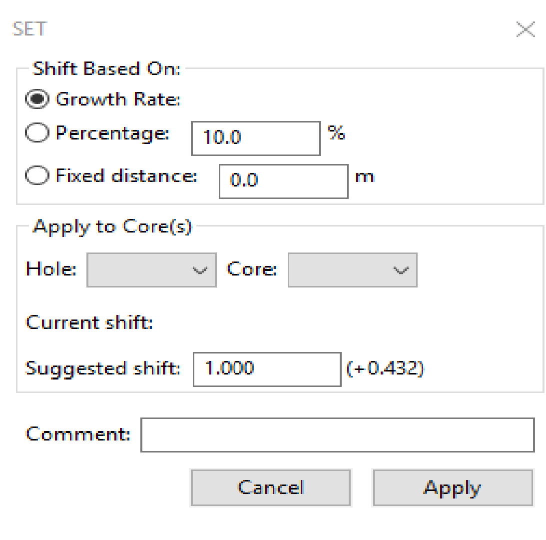

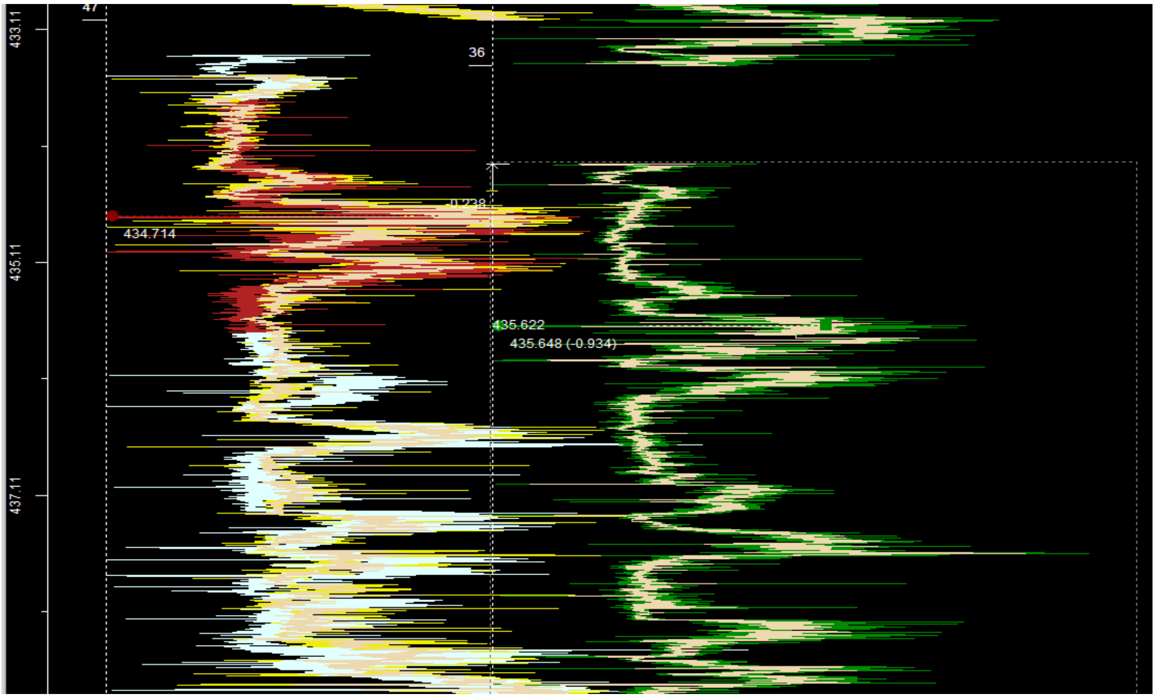

Creating the composite point, showing the correlated overlay (white and red lines), and correlating the peaks.

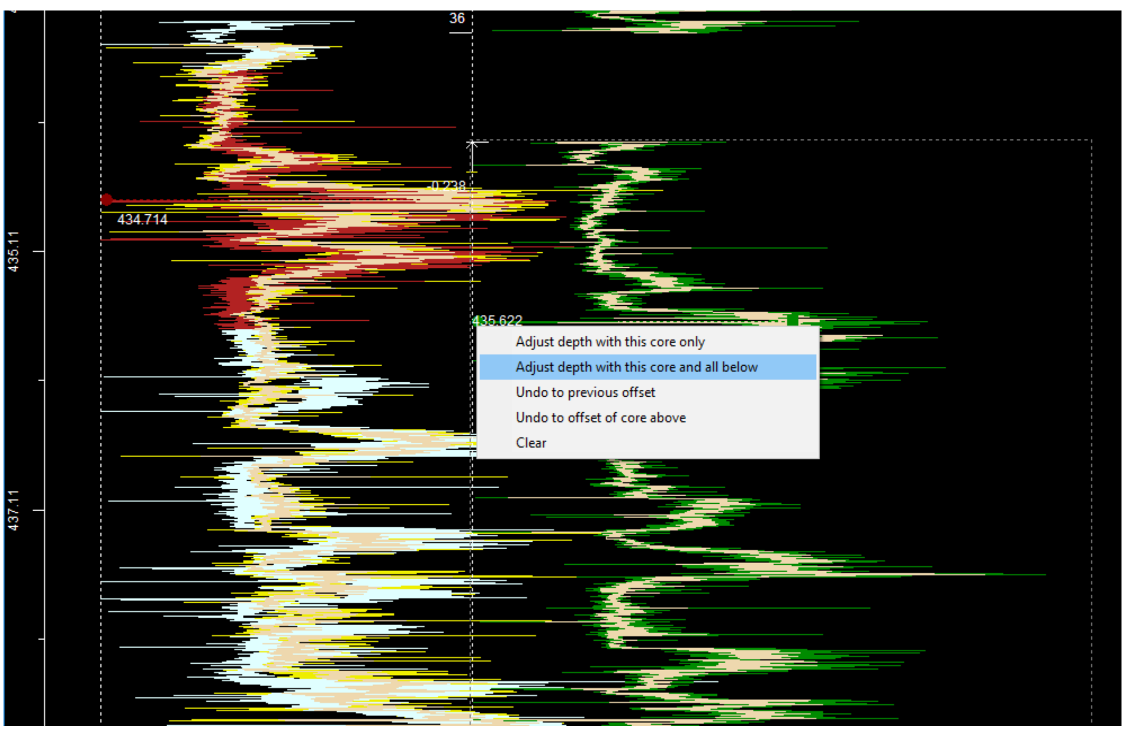

When you are done correlating, go to the Tool Bar in the Display or Data Manager, click save, and choose Affine Table.

Splicing Data:

After compositing the sets of data, the next step is to splice them into one composite graph.

Go to the preferences tab and check the Splice/Log Window. A second window on the right should appear with another scroll bar.

- The "second scroll" option allows you to use two different scroll bars to change depth – one for the compositing section, one for the splicing section. It seems more practical to leave this unchecked.

Go to the top of your data and **click and drag** data from one set over to the right-hand window. A mirror image of that data in blue should appear.

Then, click and drag the data from the second set over to the right-hand window, and a corresponding tan line should be created in the splice window.

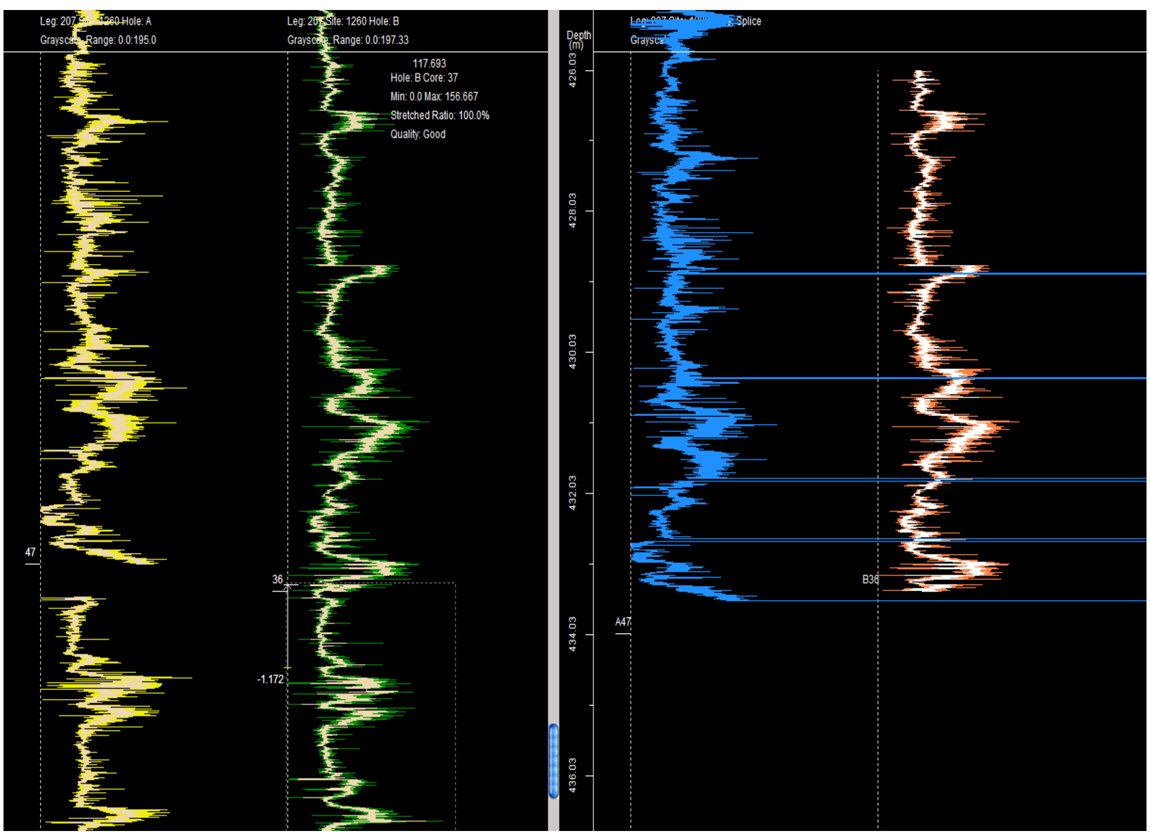

There are two methods of splicing in *Correlator* – Constrained and Unconstrained. Constrained splicing creates a fixed splice line across both sets of data. Unconstrained splicing allows you choose splice points at different depths for different sets of data (preferred).

Like compositing, to splice the data, Shift+Left Click on Set A, and Shift+Left Click on Set B to create the splice points. A reference white and red series will be overlain over the blue data to show the result of the splice at that point.

- If you are working with low resolution data, you can go to the Splice tab to view the evaluation graph that determines how good of a match the splice points are. This again does not work well with high resolution data.
- Similar to compositing, you may also have to Shift+Left Click multiple times for Correlator to actually create the splice points, especially if you are working with high resolution data.
- Splice points can be clicked + dragged the same as composite tie points.
- **If there are no points that can be spliced, see below (appending data).**

When the splice points are in the right location, right click on the green circle and choose Set.

After the splice is made, the spliced data should be added (as a new part of the blue dataset) to the gaps and/or end of your data.

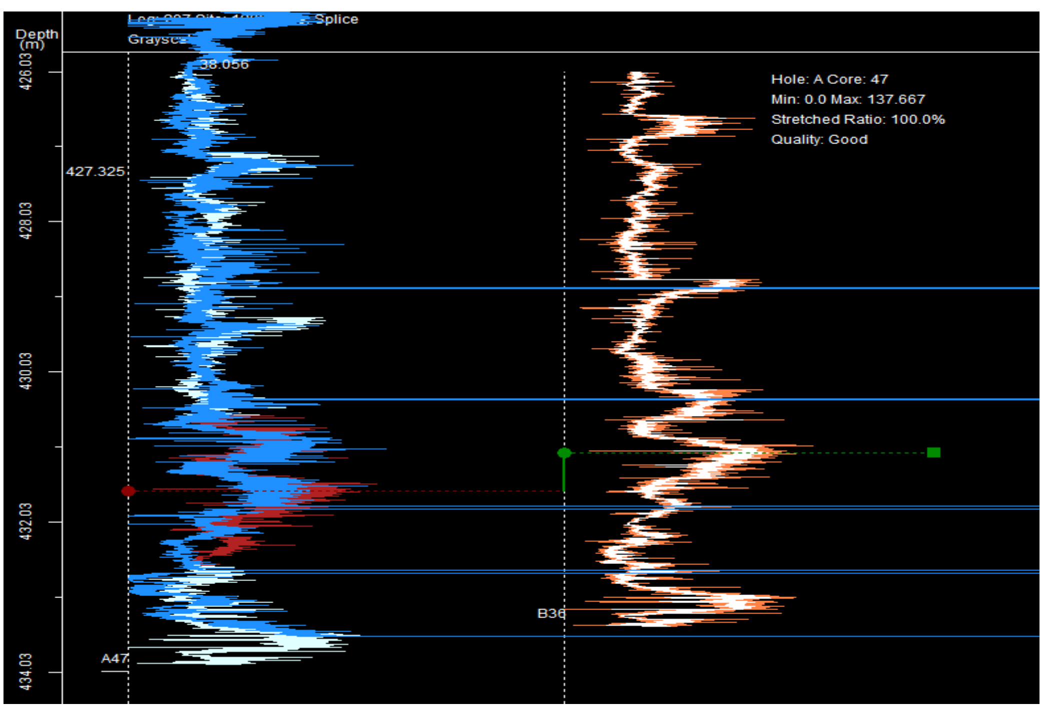

Appending Data:

In *Correlator*, you have to drag over one section from Set A, and then drag one from Set B in order to splice. **However, if there is a gap in both cores and a splice point cannot be made, you will have to "append" a core.**

- If you want to add multiple core sections consecutively from the same dataset, you will have to use this.

Appending works (primarily) in two ways, either by:

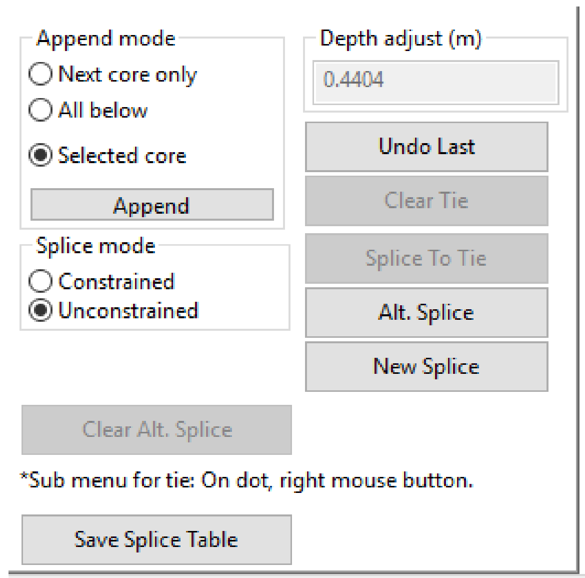

- Appending the next core only, which inserts the next core section under the previous dataset as the next part of the splice.
- Or appending the selected core, done by dragging over the core of the next dataset (which is represented in the image on the next page).
- Append all below is only used if there is one core that extends much farther than another.
- You can also undo splices in this section of the splice tab.

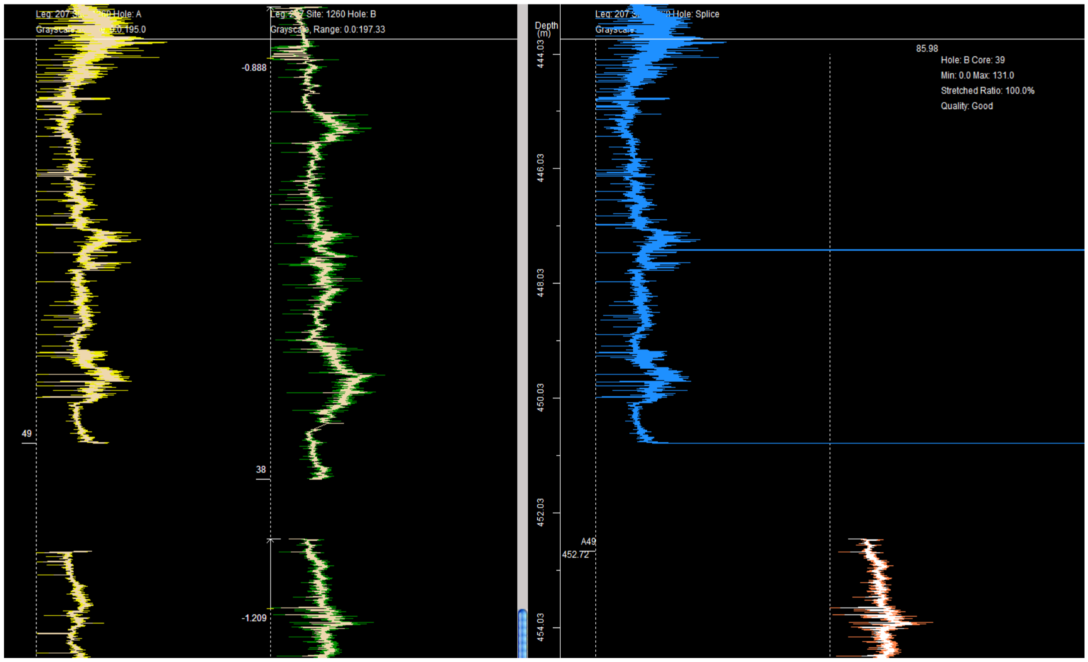

When you are done splicing, go to the toolbar and select save splice.

<u>Exporting Data:</u>

When you have finished making the composited splice graph, you can export the data by going back to the Data Manager tab.

From here, right click on your data row (i.e. Grayscale), and choose export.

Select the format you want, apply Cull, Affine, and Splice tables, and click next. You will then be prompted to choose your save location and file name.

Once more, exporting can take some time with high resolution data.

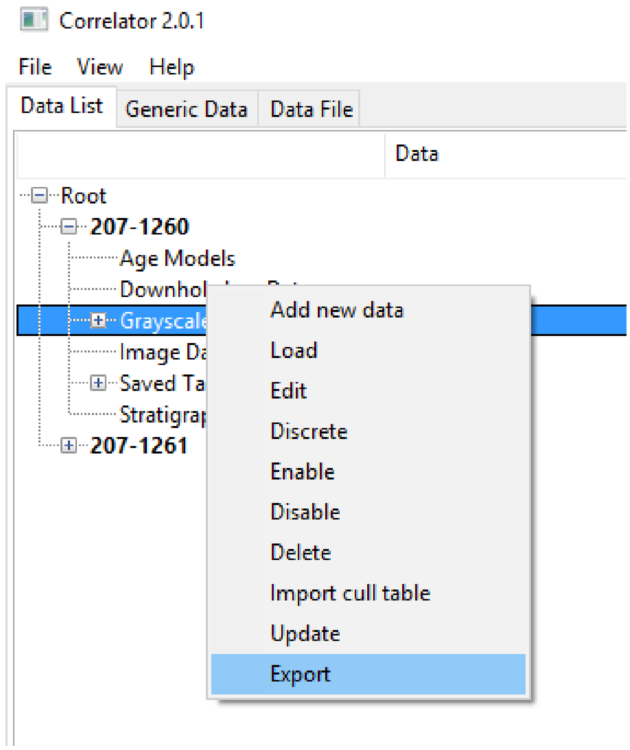

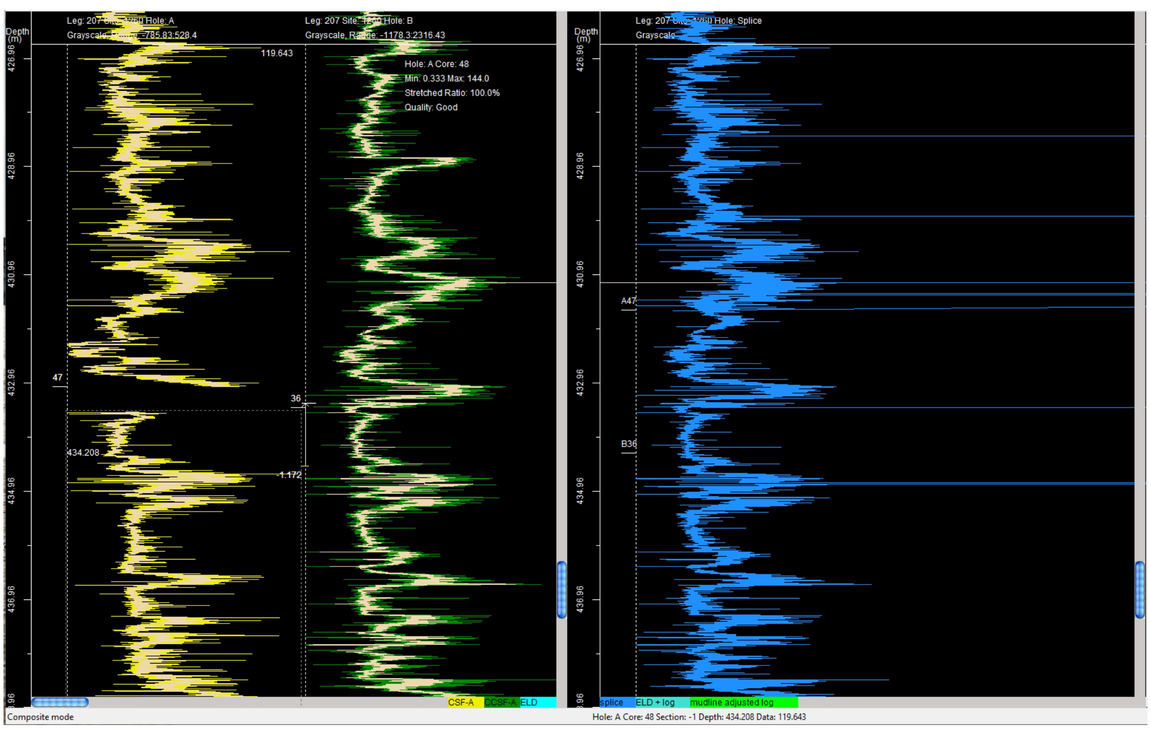

Composited section from Site 1260 showing raw grayscale data from Core A (yellow) and Core B (green) that has been shifted and spliced to create a composite (blue).

APPENDIX C

R command sequence for ASM:

```
GS <- read.csv("~/RStudio/Shale570-580.csv", header=FALSE)
library(astrochron)
ls()
plot(GS,type='l')
strats(GS)
GSint=linterp(GS,0.0059)
GSmtm=mtm(GSint,tbw=2,ntap=NULL,padfac=5,demean=T,detrend=T,siglevel=0.90,ar1
=F,output=3,CLpwr=F,xmin=0,xmax=10,pl=2,sigID=T,genplot=T,verbose=T)
View(GSmtm)
freq=GSmtm$Frequency
• Find X number of significant peaks < 5 cycles/m according to MTM f-test output
freqs<-freq[1:X]
target=c(1/405.47,1/126.98,1/96.91,1/37.66,1/22.42,1/18.33)
• Set X Rayleigh frequency given MTM; set Nyquist = 10
asm(freqs,target,fper=NULL,rayleigh=X,nyquist=10,sedmin=0.1,sedmax=5,numsed=100,l
inLog=1,iter=1000,output=T,genplot=T)
```

APPENDIX D

MATLAB command sequences for prewhitening and spectral analysis

MATLAB commands to generate the prewhitened grayscale series and evolutionary FFT spectrogram

• Analyze spacing of grayscale depth sampling
> diffd=diff(shalegrayscaleclean(:,1));
> mean(diffd)
> min(diffd)

• Plot and zoom the y-axis to be from 0 to 0.001
> figure; plot(diffd);
> dint=0.0059;
> len=length(shalegrayscaleclean(:,1);
> depthint=shalegrayscaleclean(1,1):dint:shalegrayscaleclean(len,1);
> grayscaleint=interp1(shalegrayscaleclean(:,1),shalegrayscaleclean(:,2),depthint);

• Pre-whiten the interpolated series in preparation for spectral analysis and test smoothers
> span10=10./dint;
> span20=20./dint;
> smooth10=smooth(grayscaleint,span10,'loess');
> smooth20=smooth(grayscaleint,span20,'loess');
> figure; plot(depthint, grayscaleint); hold all; plot(depthint,smooth101260); hold all; plot(depthint,smooth201260);

• Remove smoother from data and plot residual
> grayscaleint=grayscaleint’;
> grayscaleres=grayscaleint-smooth20;
> figure; plot(depthint,grayscaleres);

APPENDIX E

MATLAB command sequence for multitaper power spectrum and FFT spectrogram

• Download evofft.m from http://mason.gmu.edu/~lhinnov/cyclotools/

• 2pi MTM power spectrum
> [p1260,w1260]=pmtm(grayscaleres,2);
> f1260=w1260/(2*pi*dint);

• Plot and restrict frequency axis to [0,5], and identify the wavelengths of all prominent peaks
> figure; plot(f1260,p1260);

• Create Evolutionary FFT spectrogram
> depthint=depthint'
> grayscaleresall=[depthint,grayscaleres];
> window=10.; step=0.2; fmin=0.; fmax=5.;
> s=evofft(grayscaleresall,window,step,dint,fmin,fmax,'m');

MATLAB command sequence for Laskar 2004 eccentricity FFT spectrogram

> load('la2004eccentricity.txt');
> dt=(la2004eccentricity(2,1)- (la2004eccentricity(1,1)));
> figure; plot(la2004eccentricity(:,1), la2004eccentricity(:,2));

• Compute 2pi MTM power spectrum, remove mean value first
> la2004eccm= la2004eccentricity(:,2)- mean(la2004eccentricity(:,2));
> [pecc,wecc]=pmtm(la2004eccm,2);
> fecc=wecc/(2*pi*dt);
> figure;plot(fecc,pecc);
> window=500; step=dt; fmin=0.;fmax=0.05;
> s=evofft(la2004eccm,window,step,dt,fmin,fmax,'kyr');

REFERENCES

Alvarez, W., and Sannipoli, E. (2016), Guido Bonarelli and the geological discovery of the Bottaccione Gorge at Gubbio, in Menichetti, M., Coccioni, R., and Montanari, A., eds., The Stratigraphic Record of Gubbio: Integrated Stratigraphy of the Late Cretaceous–Paleogene Umbria-Marche Pelagic Basin, Geological Society of America Special Paper 524, p. 1–11, doi:10.1130/2016.2524(01).

Arthur, M.A., Dean, W.E., and Pratt, L.M. (1988), Geochemical and climatic effects of increased marine organic carbon burial at the Cenomanian/Turonian boundary, *Nature*, v. 335, p. 714–717.

Basile, B., Maillard, A., Patriat, M., Gaullier, V., Loncke, L., Roest., W, de Lepinay, M.M., and Pattier, F. (2013), Structure and evolution of the Demerara Plateau, offshore French Guiana: rifting, tectonic inversion and post-rift tilting at transform-divergent margins intersection, *Tectonophysics,* v. 591, p. 16-29.

Berger, A., Loutre, M. F., and Laskar, J. (1992), Stability of the astronomical frequencies over the Earth's history for paleoclimate studies, *Science*, v. 255, p. 560-566.

Black, M. (1972), British lower Cretaceous coccoliths. I-Gault Clay (Part 1). *Palaeontographical Society Monograph*, v. 126, p. 1-48.

Bralower, T.J., Bown, P.R., Erba, E., Jenkyns, H., Leckie, M., Robinson, S. (2013), A workshop aimed at advancing our understanding of Cretaceous ocean dynamics by scientific ocean drilling, Bloomsbury, London, United Kingdom.

Bown, P.R. (1998), Calcareous nannofossil biostratigraphy, *Calcareous Nannofossil Biostratigraphy, Kluwer Academic*, 315 p.

Burnett, J.A., (1998), Upper Cretaceous. In: Bown, P.R. (Editor), Calcareous Nannofossil Biostratigraphy. *British Micropalaeontological Society Publication Series*, p. 132-199.

Eldrett, J.S., Minisini, D., and Bergman, S.C. (2014), Decoupling of the carbon cycle during Ocean Anoxic Event 2, *Geology*, v. 42, p. 567-570.

Eldrett, J.S., Ma, C., Bergman, S.C., Lutz, B., Gregory, F.J., Dodsworth, P., Phipps, M., Hardas, P., Minisini, D., Ozkan, A., Ramezani, J., Bowring, S., Kamo, S.L., Ferguson, K., Macaulay, C., and Kelly, A.E. (2015), An astronomically calibrated stratigraphy of the Cenomanian, Turonian and earliest Coniacian from the

Cretaceous Western Interior Seaway, USA: Implications for global chronostratigraphy, *Cretaceous Research*, v. 56, p. 316-344.

Erbacher, J., Huber, B.T., Norris, R.D., and Markey, M. (2001), Increased thermohaline stratification as a possible cause for an ocean anoxic event in the Cretaceous period, *Nature*¸ v. 409, p. 325-327.

Erbacher, J., Friedrich, O., Wilson, P.A., Birch, H., and Mutterlose, J. (2005), Stable organic carbon isotope stratigraphy across Oceanic Anoxic Event 2 of Demerara Rise, western tropical Atlantic, *Geochemistry, Geophysics, Geosystems,* v. 6, p. 1-9.

Gouyet, S., Unternehr, P., and Mascle, A., (1994), The French Guyana margin and the Demerara Plateau: geological history and petroleum plays, in: Mascle, A. (ed), *Hydrocarbon and petroleum geology of France*, p. 411-422.

Greenroyd, C.J., Pierce, C., Rodger, M., Watts, A.B., and Hobbs, R.W. (2008), Demerara Plateau – the structure and evolution of a transform passive margin, *Geophysical Journal International*, v. 172, p. 549-564.

Hardas, P., and Mutterlose, J. (2006), Calcareous nannofossil biostratigraphy of the Cenomanian/Turonian boundary interval of ODP Leg 207 at the Demerara Rise, *Reviews in Micropaleontology.,* v. 49, p. 165-179.

Hay, W.W., 2017. Toward understanding Cretaceous climate—An updated review. *Science China Earth Sciences*, v. 60, p. 5-19, doi:10.1007/s11430-016-0095-9

Hays, J.D., Imbrie, J., and Shackleton, N.J. (1976), Variations in the Earth's orbit: pacemaker of the ice ages, *Science*, v. 194, p. 1121-1132.

Hinnov, L.A. (2013), Cyclostratigraphy and its revolutionizing applications in the earth and planetary sciences, *Geological. Society of. America Bulletin,* v. 125, 1703-1734.

Hinnov, L.A., and Hilgen, F. (2012), Chapter 4: Cyclostratigraphy and Astrochronology, in Gradstein, F.M., Ogg, J., Schmitz, M., and Ogg, G., eds., The Geologic Time Scale 2012, Elsevier, p. 63-83.

Hinnov, L.A., Wu, H., and Fang, Q. (2016), Reply to the comment on "Geologic evidence for chaotic behavior of the planets and its constraints on the third-order eustatic s..., *Palaeogeography, Palaeoclimatology, Palaeoecology*, http://10.1016/j.palaeo.2016.07.030

Imbrie J. & Imbrie K. P. (1979), Ice Ages: Solving the Mystery. Macmillan Publishers, 224 p.

Kennedy, W. J., Walaszczyk, I., and Cobban, W.A. (2005), The Global Boundary Stratotype Section and Point for the base of the Turonian Stage of the Cretaceous: Pueblo, Colorado, U.S.A., *Episodes*, v. 28, p. 93-104.

Kodama, K.P., and Hinnov, L.A. (2015), Rock Magnetic Cyclostratigraphy, New Analytical Methods in Earth and Environmental Science series, doi:10.1002/9781118561294

Kolonic, S., Wagner, T., Forster, A., Sinninghe Damsté, J.S., Walsworth-Bell, B., Erba, E., Turgeon, S., Brumsack, H.J., Chellai, E.H., Tsikos, H., Kuhnt, W., and Kuypers, M.M.M (2005), Black shale deposition on the northwest African Shelf during the Cenomanian/Turonian oceanic anoxic event: Climate coupling and global organic carbon burial, *Paleoceanography*, v. 20.

Lanci, L., Muttoni, G., and Erba, E. (2010), Astronomical tuning of the Cenomanian Scaglia Bianca Formation at Furlo, Italy, *Earth and Planetary Science Letters*, v. 292, p. 231-237.

Larson, R.L. (1991a). Latest pulse of Earth: Evidence for a mid-Cretaceous superplume, *Geology*, v. 19, p. 547-550Larson, R. L. (1991b). Geological consequences of superplumes, *Geology*, v. 19, p. 963-966.

Li, Y.X., Montañez, I.P., Liu, Z., and Ma, L. (2017), Astronomical constraints on global carbon-cycle perturbation during Oceanic Anoxic Event 2 (OAE2), *Earth and Planetary Science Letters.,* v. 462, p. 35-46.

Littler, K., Robinson, S.A., Bown, P.R., Nederbragt, A.J., and Pancost, R.D. (2011), High sea-surface temperatures during the Early Cretaceous Epoch, *Nature Geoscience*, v. 4, p. 169-172.

Manivit, H., & others, (1977), Mid Cretaceous calcareous nannofossil biostratigraphy, *Proceedings of the Koninklijke Nederlandse Akademie van Wetenschappen*, v. 80, p. 169-181.

Ma, C., Meyers, S.R., and Sageman, B.B. (2017), Theory of chaotic orbital variations confirmed by Cretaceous geological evidence, *Nature*, v. 542, p. 468-472, doi:10.1038/nature21402

Marzoli, A., Renne, P.R., Piccirillo, E.M., Ernesto, M., Bellieni, G., De Min, A. (1999), Extensive 200 million-year-old continental flood basalts of the central Atlantic magmatic province, *Science* v. 284, p.616-618

Meyers, S.R., and Sageman, B.B. (2007), Quantification of Deep-Time Orbital Forcing by Average Spectral Misfit: *American Journal of Science*, v. 307, p. 773-792.

Meyers, S.R., Siewert, S.E., Singer, B.S., Sageman, B.B., Condon, D.J., Obradovich, J.D., Jicha, B.R., and Sawyer, D.A., (2012a), Intercalibration of radioisotopic and astrochronologic time scales for the Cenomanian–Turonian boundary interval, Western Interior Basin, USA, *Geology*, v. 40, p. 7-10.

Meyers, S.R., Sageman, B.B., and Arthur, M.A., (2012b), Obliquity forcing of organic matter accumulation during Oceanic Anoxic Event 2, *Paleoceanography,* v. 27.

Meyers, S.R., (2014), Astrochron: An R package for astrochronology. https://cran.r-project.org/package=astrochron

Meyers, S.R., (2016), The Integration and intercalibration of radioisotopic and astrochronologic time scales, *Isoastro Geochronology Workshop*, Boise, Idaho, August 15-20, 2016.

Miller, K. G., Kominz, M.A., Browning, J.V., Wright, J.D., Mountain, G.S., Katz, M.E., Sugarman, P.J., Cramer, B.S., Christie-Blick, N., and Pekar, S.F. (2005), The Phanerozoic record of global sea-level change, *Science*, v. 310, p. 1293-1298.

Mitchell, R.N., Bice, D.M., Montanari, A., Cleaveland, L.C., Christianson, K.T., Coccioni, R., and Hinnov, L.A. (2008), Ocean anoxic cycles? Prelude to the Livello Bonarelli (OAE 2), Earth and Planetary Science Letters, v. 267, p. 1-16.

Müller, D.R., Sdrolias, M., Gaina, C., Steinberger, B., and Heine, C. (2008), Long-term sea-level fluctuations driven by ocean basin dynamics, *Science*, v. 319, p. 1357-1362.

Nederbragt, A., Fiorentino, A., (1999), Stratigraphy and palaeoceanography of the Cenomanian–Turonian boundary event in Oued Mellegue, north-western Tunisia, *Cretaceous Research* v. 20, p. 47-62.

Nederbragt, A.J., Thurow, J., and Pearce, R., (2007), Sediment composition and cyclicity in the mid-Cretaceous at Demerara Rise, ODP Leg 207. In Mosher, D.C., Erbacher, J., and Malone, M.J. (Eds.), *Proc. ODP, Sci. Results*, v. 207: College Station, TX (Ocean Drilling Program), p. 1–31.

Ogg, J.G., and Hinnov, L.A., (2012), Chapter 27: The Cretaceous, in: Gradstein, F.M., Ogg, J.G., Schmitz, M. and Ogg, G., eds., The Geologic Time Scale 2012, Elsevier, p. 793-853, doi:10.1016/B978-0-444-59425-9.00027-5.

Percival, F.B., and Walden, A.T. (1993), Spectral Analysis for Physical Applications, Cambridge University Press, Cambridge, 583 p.

Poulsen, J.P., Barron, E.J., Arthur, M.A., and Peterson, W.H. (2001), Response of the mid-Cretaceous global oceanic circulation to tectonic and CO2 forcings, *Paleoceanography*, v. 16, p. 576-592.

Prokoph, A., Villenueve, M., Agterberg, F.P., and Rachold, V. (2001), Geochronology and calibration of global Milankovitch cyclicity at the Cenomanian-Turonian boundary, *Geology*, v. 29, p. 523-526.

Schlanger, S.O., and Jenkyns, H.C. (1976), Cretaceous oceanic anoxic events: Causes and consequences, *Geologie en Mijnbouw*, v. 55, p. 179-184.

Shipboard Scientific Party, (2004), Leg 207 summary, *Proc. ODP Initial Reports*, v. 207. p. 1-89.

Thomson, D.J. (1982), Spectrum estimation and harmonic analysis. *Proc. IEEE*, v. 70,p. 1055-1096.

Turgeon, S.C., and Creaser, R.A. (2008), Cretaceous oceanic anoxic event 2 triggered by a massive magmatic episode, Nature, 454, 323-326, doi:10.1038/nature07076

Thomson, D.J. (2009), Time-series analysis of paleoclimate data. In: Gornitz, V. (Ed.), *Encyclopedia of Paleoclimatology and Ancient Environments*, p. 949-959.

Tsikos, H., Jenkyns, H.C., Walsworth-Bell, B., Petrizzo, M.R., Forster, A., Kolonic, S., Erba, E., Premoli Silva, I., Baas, M., Wagner, T., and Sinninghe Damsté, J.S. (2004), Carbon-isotope stratigraphy recorded by the Cenomanian-Turonian Oceanic Anoxic Event: Correlation and implications based on three localities, *Journal of the Geological Society of London,* v. 161, p. 711-719.

Voigt, S., Gale, A., Kennedy, W.J., and Walaszczyk, I.P. (2005), Stratigraphy of the Late Cenomanian-Early Turonian chalk succession at Eastbourne, Sussex, UK: ammonites, inoceramid bivalves and stable carbon isotopes, *Cretaceous Research*, v. 26, p. 460-487.

Wang, Y., Huang, C., Sun, B., Quan, C., Wu, J., and Lin, Z., 2014. Paleo-CO_2 variation trends and the Cretaceous greenhouse climate, Earth-Science Reviews, 129, 136-147, doi:10.1016/j.earscirev.2013.11.001

BIOGRAPHY

Sean E. Karoly graduated from Oakton High School in Oakton, Virginia, in 2011. He attended Radford University in Radford, VA, where he earned his Bachelor of Science in Geology in 2015. He then attended George Mason University in Fairfax, VA, and received his Master of Science in 2017. He has worked as a physical science trainee at the United States Geological Survey in Reston, VA, and as a research assistant with George Mason University in 2016. He has been employed as a part-time intern at the Mineralogical Society of America in Chantilly, VA since 2014.